Drying of Spent Advanced Gas Reactor Fuel

Thomas Bainbridge*[1], Prof. Bruce Hanson[1], Dr Nicole Hondow[1], Dr Carlos de la Fontaine[2]
[1]University of Leeds, [2]TÜV SÜD Nuclear Technologies
*pmtoba@leeds.ac.uk

Project Background

Fig 1. AGR Fuel Assembly [1]

Current Spent Fuel Strategy:

With the UK deciding to cease reprocessing, spent fuel is being interim stored pending a decision on whether to classify the spent fuel as waste for disposal [2].

This is expected to be a Geological Disposal Facility in 2075 with wet interim storage being the preferred option with dry storage being investigated as an alternative as well as a prerequisite for disposal.

While in wet storage there is a risk of the cladding corroding and leading to water seeping in.

To reduce the risk of corrosion the storage ponds are dosed to pH 11.4

Why Do We Need To Dry Spent Fuel?

If water that has become entrained in the fuel is not removed then radiolysis will occur.

This will produce H_2 and H_2O_2. Hydrogen is flammable and explosive while the hydrogen peroxide will further corrode the cladding and exacerbate the issue.

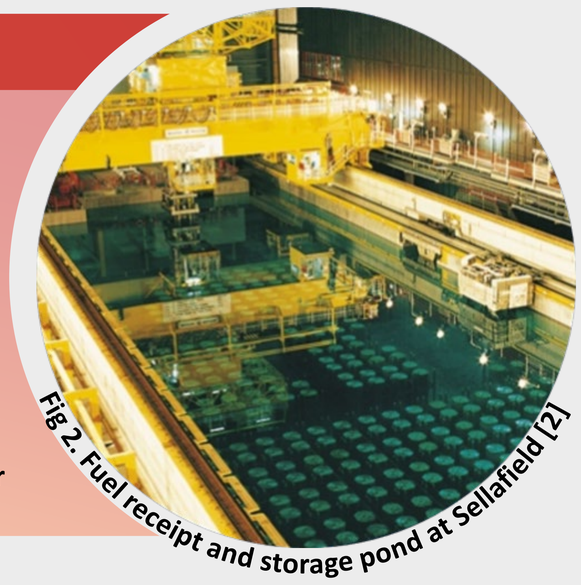

Fig 2. Fuel receipt and storage pond at Sellafield [2]

Cracking Stainless Steel

In order to corrode samples and produce representative cracks in stainless steel a drop evaporation test is being performed.

Samples of 304 stainless steel were sensitised at 600°C for 5 hours before being furnace cooled.

35g/L NaCl dripped onto the sample which is heated to 180°C allowing the previous drop to evaporate before the next drop falls [5-8].

Tests so far have had durations of 14, 21 and 28 days, with longer tests planned with NaCl and other salts such as $FeCl_3$ and $AlCl_3$.

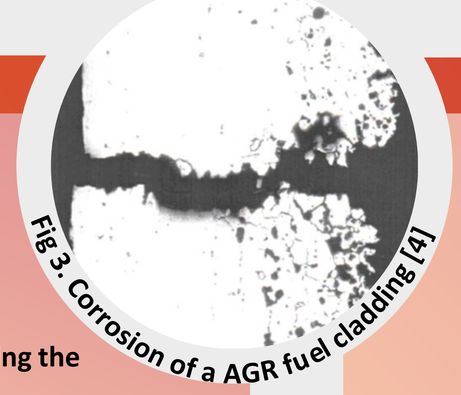

Fig 3. Corrosion of a AGR fuel cladding [4]

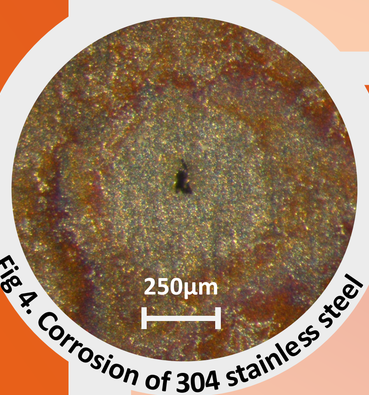

Fig 4. Corrosion of 304 stainless steel

Corrosion Experimental Set Up

Clean samples showed minimal signs of corrosion following 14 days of exposure under test conditions.

To try and increase the corrosion rate a centre punch has been used to create small pits in the surface.

Multiple pits of around 50µm have been observed and CT scans are being looked at.

However, due to the dimensions of the expected cracks (1-10µm) this is proving hard.

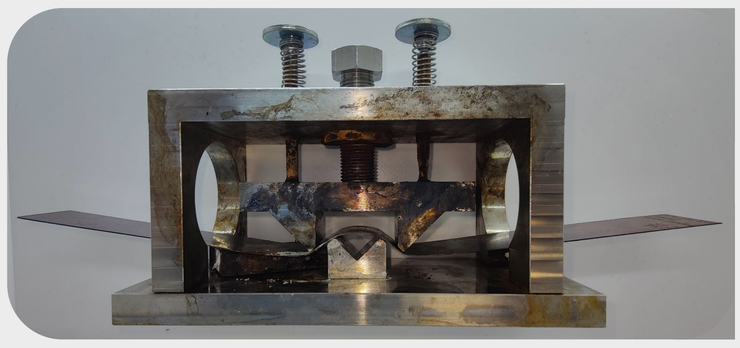

Fig 5. Drop Evaporation Test rig set up

Process Model

Factors being considered for the process model

1. Vacuum pump down of the chamber
2. Flow through the crack
3. Evaporation of the water in the sample
4. Heating of the sample

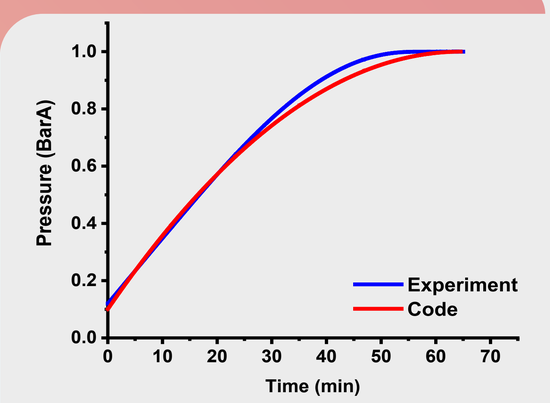

Fig 7. Code vs Pinhole Experiment

When considering the evaporation of water the vapour pressure is found for the conditions inside the sample at each time step value. The water mass is then reduced by the number of moles required to reach the vapour pressure.

The vapour pressure is calculated using the Clasius-Clapeyron equation given as [9] :

$$\ln\left(\frac{P_1}{P_2}\right) = -\frac{\Delta H_{vap}}{R} \cdot \left(\frac{1}{T_1} - \frac{1}{T_2}\right)$$

The flow velocity, u, is given by the following equation where inertia becomes more important as the flow takes a less tortuous route through the crack corresponding to regime 2 in the paper [10].

$$0 = \frac{\rho \cdot u^2}{2} \cdot \left[N \cdot 2 \cdot \theta \cdot \frac{d_{eff}}{d}\right] + \frac{2 \cdot u}{\rho} \cdot \left[\frac{12 \cdot \mu \cdot \ell_{eff}}{d_{eff}^2}\right] - \Delta P$$

With the volumetric flow then given by

$$Q = u \cdot d_{eff}$$

Flow Rate

To obtain the flow rate through various sizes of pinholes) a rig has been constructed to remove as many factors that could affect the flow.

The diameters of the pinholes being investigated are 100µm, 50µm, 20µm, 10µm, 5µm & 1µm. Current results suggest that below 20µm the flow rate becomes so low as to be impractical for testing.

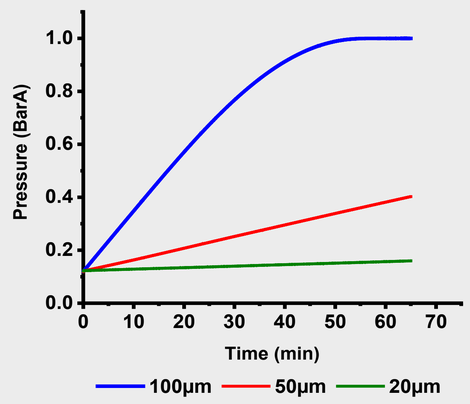

Fig 6. Comparison of different pinholes

The experimental set-up consists of a sample cylinder connected to a vacuum pump on one side and a Swagelok® fitting housing the pinhole disc.

These discs are 0.025mm thick stainless steel sealed into the fitting with an O-ring and backed by a steel plate to prevent it from deforming.

Tests to measure the evaporation of water in a vacuum are also being conducted

Vacuum Drying

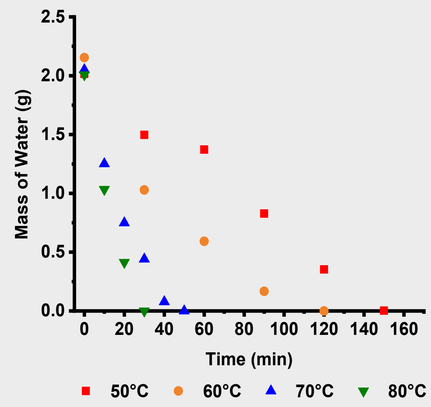

Fig 8. Drying Rig Mass Removed Graph

The final set of experiments being carried out is to conduct vacuum drying of samples.

Currently pinhole tests have been run with a view to providing initial validation of the process model.

Once cracks have been produced they will be used to create samples to be used in this experiment.

As the experiment is being carried out the sample can be weighed to track the mass lost over the course of the run.

In addition to this the mass flow rate, pressure and dew point are all recorded which can allow for additional validation points.

References

[1] Science Museum Group. AGR Fuel Element, c 1982. 1982-1575Science Museum Group Collection Online. Accessed May 27, 2022. https://collection.sciencemuseumgroup.org.uk/objects/co5473/agr-fuel-element-c-1982-nuclear-fuel-fuel-rods.
[2] Nuclear Decommissioning Authority. Oxide Fuels - Preferred Option - Publications - GOV.UK. Technical Report SMS/TS/C2-OF/001/Preferred Option, June 2012. URL https://www.gov.uk/government/publications/oxide-fuels-preferred-option.
[3] https://processengineering.co.uk/article/2012839/sellafield-nuclear-r
[4] J. Kyffin and A. Hillier (2015). "Technological Development to Support a Change in the United Kingdom's Strategy for a Management of Spent AGR Oxide Fuel." International Conference on Management of Spent Fuel from Nuclear Power Reactors.
[5] Pereira, H. B., et al. (2019). "Investigation of stress corrosion cracking of austenitic, duplex and super duplex stainless steels under drop evaporation test using synthetic seawater." Materials Research 22(2).
[6] Drugli, J. M. and Steinsmo, U. (no date) 'Assessment of Suscetibility to Chloride Stress Corrosion Cracking of Highly Alloyed Stainless Steels. Part II: A New Immersion Test Method', (194)
[7] Lasek, S., CÍHAL, V. and Blahetová, M. (2002) 'Stress corrosion cracking study of austenitic stainless steels by the drop evaporation test', in *Sb. konf.*
[8] Parrott, R., Pitts, H. and Hill, H. D. (2011) 'Chloride stress corrosion cracking in austenitic stainless steel', *The Health and Safety Laboratory for the Health and Safety Executive: Buxton, UK.*
[9] Koutsoyiannis, D. (2012) 'Clausius-Clapeyron equation and saturation vapour pressure: Simple theory reconciled with practice', *European Journal of Physics*, 33(2), pp. 295–305. doi: 10.1088/0143-0807/33/2/295.
[10] Beck, S., et al. (2005). "Explicit equations for leak rates through narrow cracks." International journal of pressure vessels and piping 82(7): 565-570.

Acknowledgements

Academic Supervisors: Prof. Bruce Hanson, Dr Nicole Hondow
Industrial Supervisor: Dr Carlos de la Fontaine

NUCLEAR ENGINEERING University of Leeds
UNIVERSITY OF LEEDS

Transformative Science and Engineering for Nuclear Decommissioning

Engineering and Physical Sciences Research Council
Energy For a Low Carbon Future

Electrokinetic Remediation and Decommissioning – an update on current work

Frances M. Burrell, Andy B. Cundy, Phil E. Warwick, Jamie M. Purkis, Ian T. Burke, Richard I. Marsh, Shaun D. Hemming, Arianna G. Pagano, Rebecca J. Lunn
Frances.Burrell@noc.soton.ac.uk, A.Cundy@noc.soton.ac.uk
University of Southampton, National Oceanography Centre Southampton, European Way, Southampton, SO14 3ZH

What is Electrokinetic Remediation?

The use of electricity to migrate and concentrate pollutants around an electrode in order to minimise the volume of contaminated material.

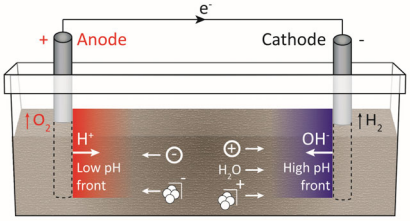

Electromigration:
Cations → cathode
Anions → anode

Electrophoresis:
+ charged particles → cathode
- charged particles → anode

Electro-osmosis
Water → cathode

The advantages of electrokinetic remediation include its adaptability to different waste matrices and the potential to be combined with other waste minimisation techniques such as bio/phyto remediation, in-situ barrier formation or colloidal grouting.

Difficult-to-measure radionuclides in cementitious materials

For more information on this project, including some preliminary results, please visit **Shaun Hemming's** poster

In this project, we are investigating whether an embedded electrode can be used to move five disparate radionuclides through cementitious material. To simplify the system, we cast a mortar using cement powder and water only and used graphite as the embedded electrode. Future work could therefore look at the effect of grain boundaries within concrete by introducing aggregate or sand into the solid matrix as well as utilising features commonly found in building structures (e.g. steel rebar) as an electrode.

Experimental set-up

- Radionuclides added: ^{137}Cs, ^{3}H, ^{236}U, ^{129}I, ^{90}Sr
- Cylindrical block dimensions:
  diameter = 12 cm, height = 7 cm
- Central electrode: graphite (diameter = 1 cm)
- External electrode: steel wire mesh fence
  (2 cm away from face of cementitious block)
- Curing time = 28 days
- Applied voltage density = 0.5 V/cm
- Electrolyte = 0.1 M NaOH
- EKR experimental duration = 6 weeks

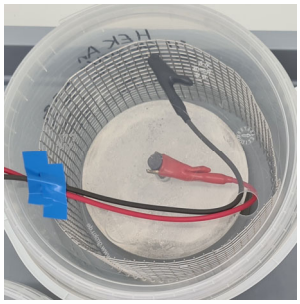

We split the tests into **two sets** to simulate two types of radionuclide contamination. For one set, **surface adsorption** of radionuclides was achieved by soaking uncontaminated blocks in a solution containing a known concentration of analytes. In the other set, radionuclides were **incorporated homogenously** throughout the block by introducing them into the cement powder and water mixture prior to casting into the moulds.

Within each set, two blocks were subjected to an **applied voltage** (anode in centre and cathode in centre), one block was left in the electrolyte solution with no applied voltage to monitor **diffusive transport,** and a final block was left untreated to quantify **initial radionuclide distribution**.

Data to be obtained

Information recorded during EKR trials:
- pH
- Current
- Appearance

Analysis after EKR trials:
- Concentration of radionuclides in soaking solutions and electrolytes
- Radial distribution of radionuclides within cementitious block
  - Quantitative (1 cm subsampling)
  - Qualitative (autoradiography)

Treatment of invasive plant species

Working with two external SMEs, we are exploring the potential to use a low applied voltage to remove invasive plant species from radiologically contaminated sites where disturbing soil could lead to redistribution of activity and/or physical removal of soil is not possible.

Electrical treatment is also more **environmentally friendly** than traditional elimination methods using chemical herbicides and is **effective throughout the annual growing cycle** of the target weed.

Image copyright: rootwave

Electrical treatment of weeds is already commercially available using the RootWave™ hand-held and tractor powered systems. This technology uses a **high AC voltage** at frequencies of **18kHz** and above, converting electrical energy into **thermal energy** within the plant and boiling it from the inside out. In this project, we are instead focusing on much **lower variable voltages** that could be powered in-situ over short periods of time and is expected to have a different effect on the target weeds. Results are not yet available due to IP sensitivities.

Independent review of electrical treatment of weeds

Study carried out by RSK ADAS Ltd on behalf of the Welsh Government:
- Dock investations in grass at 3 farms
- Compared the RootWave Pro™ hand-held system with conventional herbicide treatment (and combined)
- Found that a series of 3 electrical treatments performed as well as herbicide treatment
- 1 or 2 electrical treatments was less effective

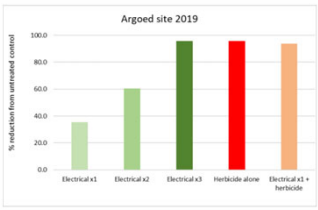

The mean % reduction from the untreated control for all treatments in experimental year one at Argoed site.

Figure from: Electrical Weed Control of Docks Final Report (30 November 2021) – ADAS for Welsh Government / EIP Wales

Electrokinetically enhanced migration of soil contaminants into silica grouting

For more information on this project, please visit **Gea Pagano's** poster

We have been working with the University of Strathclyde to combine electrokinetics with their expertise in the use of colloidal silica grouting to penetrate contaminated soil, safely containing radionuclides and generating a waste form suitable for in-situ or ex-situ vitrification.

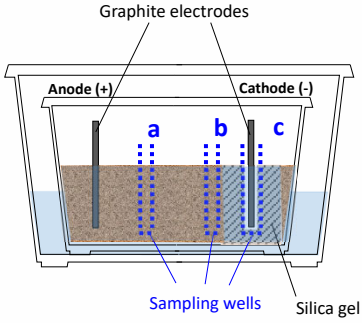

Experimental set-up

Experiments carried out so far (Strathclyde):
- Soil matrix = sand
- Analytes added: Cs and Sr
- Applied voltage density = 0.25 - 1 V/cm
- Electrolyte = 0.17 M $CaCl_2$
- EKR experimental duration up to 1 week

Future experiments (Southampton):
- Explore differently charged analytes
- Add clays/organics into the sand
- Incorporate sand/clay into the silica gel
- Simulated Sellafield groundwater as electrolyte

Experimental design and diagram by Arianna (Gea) Pagano, University of Strathclyde/Glasgow

Modifying Colloidal Silica Grout For Nuclear Decommissioning Applications

David W T Morrison[1], Matteo Pedrotti[1], Rebecca J Lunn[1], Emily R Draper[2], James Graham[3]

[1] University of Strathclyde, Department of Civil & Environmental Engineering
[2] University of Glasgow, School of Chemistry
[3] National Nuclear Laboratory, Sellafield, Cumbria

david.morrison.100@strath.ac.uk

Colloidal silica grout may greatly reduce risk of **contaminant** release in nuclear decommissioning

Here, **CS is modified** to support its use in decommissioning applications

Take a **picture** for **more info**

1. Background

Aged nuclear sites:

- **Contaminated** soil & concrete
- Deteriorated containment structures
- **Waste** to **classify** & **store** / **dispose**

Decommissioning risks **contaminant** release via…

- **Groundwater**
- **Airborne particulate**

Difficult, costly with current tech.

Colloidal Silica grout could solve **key challenges**

Aims:

- **Identify applications** for **CS**
- Modify it to best fit these

Outcomes:

- **Cost** & **time savings**
- **Reduced risk** to **workers**, **public** & **environment**

2. What is Colloidal Silica (CS)?

- **Suspension of silica nanoparticles**
- Forms **rigid gel** when mixed with **NaCl sol.**

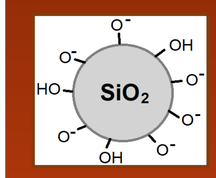

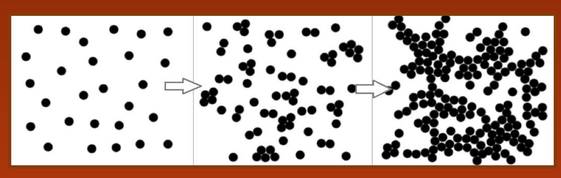

- Can inject into **soil** at low pressure so **no ground disruption**
- Used for *in situ* **hydraulic barriers.** But also…
  - **Increases soil strength**
  - **Chemically traps contaminants**

Properties:

- **Water-like viscosity**
- **Controllable gel time**
- nm particle size
- **Non-toxic, environmentally friendly**
- **Low hydraulic conductivity**

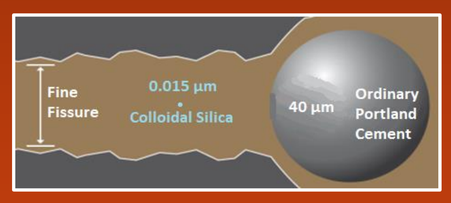

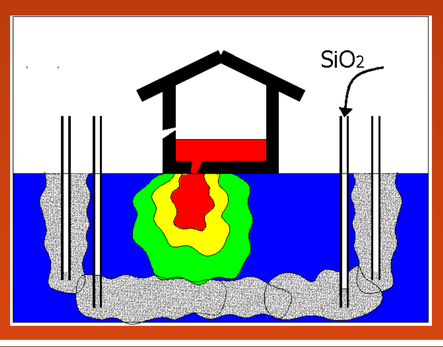

3. My Research

ENHANCED PROPERTY	IDENTIFIED APPLICATION
sorption capacity	chemical barrier
flexibility	damage resistance
compressive strength	strengthen soil waste encapsulant
re-healing	damage resistance
hydraulic conductivity	hydraulic barrier
water retention	drying resistance

FLEXIBILITY

Improved by polymer additives.

CS / POLYMER DOUBLE NETWORK

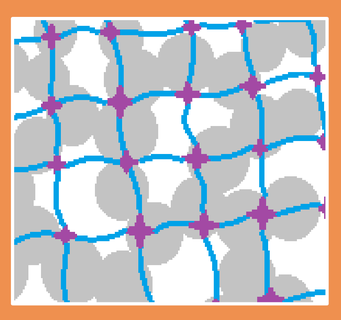

STANDARD **CS**

CS / POLYMER COMPOSITE

COMPRESSIVE STRENGTH

- **Continuous strength increase** as gel ages

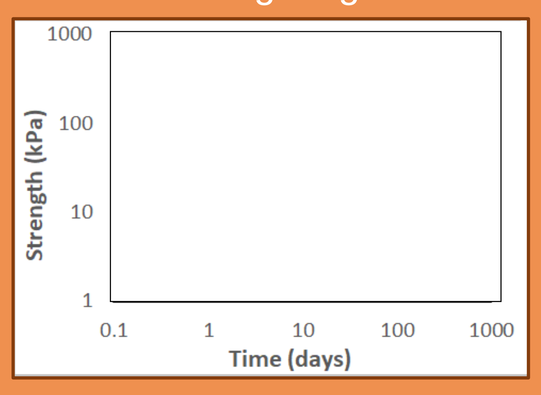

- **Increase** with **salt conc.** & **salt valency** in surroundings

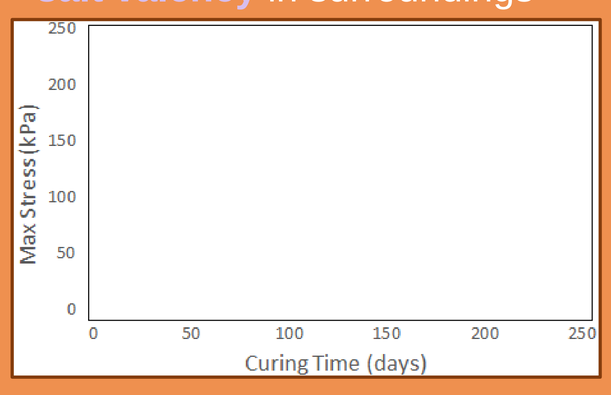

- Increase on adding **clay**
- Replace some silica to reduce cost

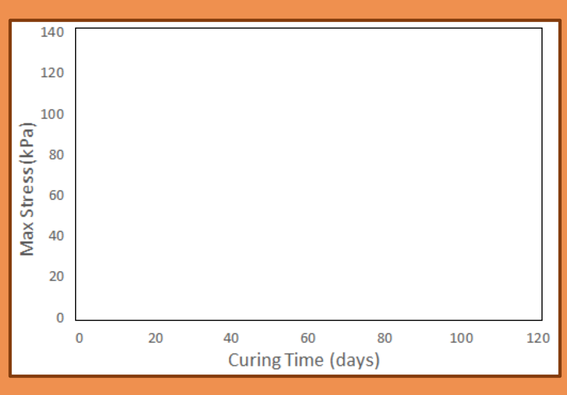

RE-HEALING

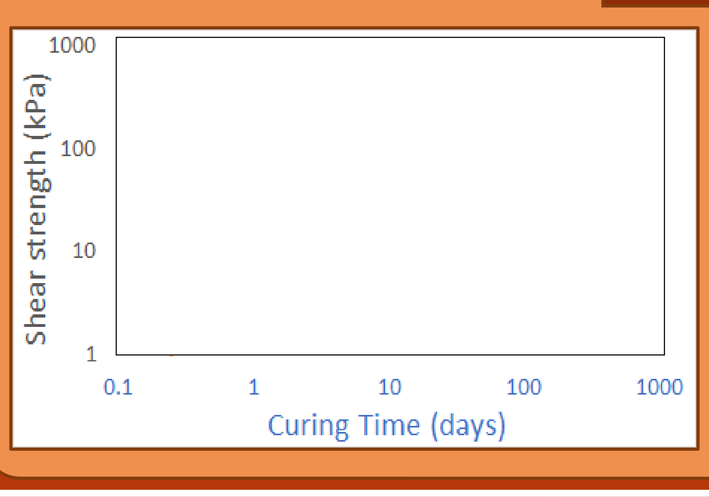

- **CS re-heals after breaking**
- **Effect strongest when gel broken early**

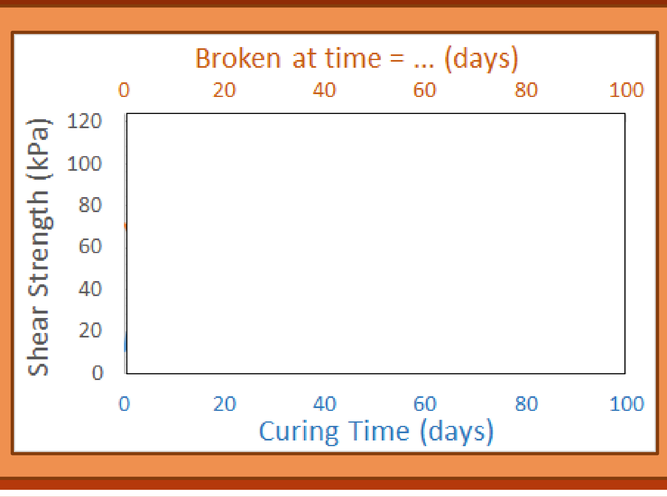

- Increased by **faster gelling**

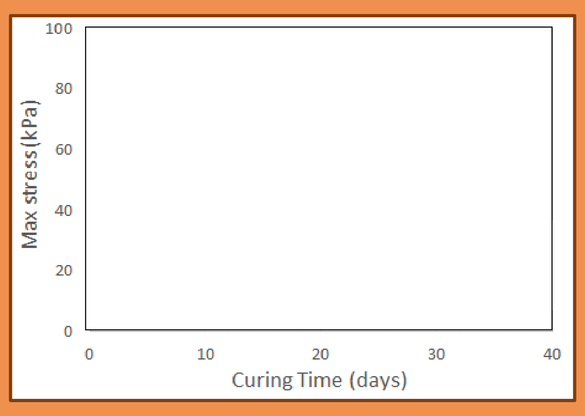

Transformative Science and Engineering for Nuclear Decommissioning

EPSRC Engineering and Physical Sciences Research Council | UK Research and Innovation

transcendconsortium.org

Energy For a Low Carbon Future

Blind tube monitoring instrument to improve the characterization of underground radioactive plumes

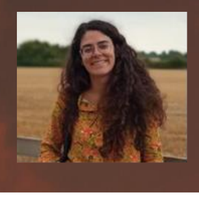

Soraia Elísio[1] (s.elisio@lancaster.ac.uk); Malcolm J. Joyce[1] (m.joyce@lancaster.ac.uk); James Graham[2] (james.graham@uknnl.com); Tom Calverley[3] (tom.calverley@sellafieldsites.com) [1]Department of Engineering, Lancaster University, Lancaster (UK); [2]National Nuclear Laboratory Ltd., Central Laboratory, Sellafield (UK); [3]Radiometric Systems Group, Sellafield Ltd., Site Management Centre, Sellafield

1. Motivation

Migration of contaminated water into the ground from legacy nuclear facilities

→ Possible contamination of groundwater & other water receptors

→ Radiological risk to public health & environment

→ Assessment of subsurface contaminated ground

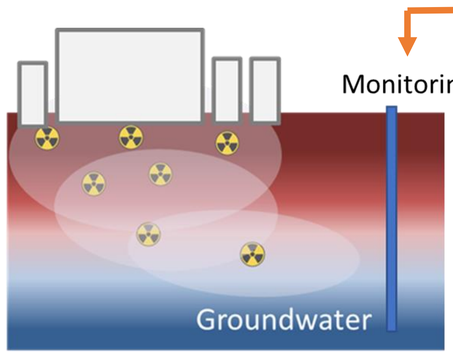

Methods to assess radioactive contaminants underground using monitoring wells

A. Groundwater sampling

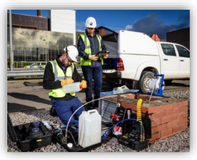

- ✓ Laboratory based instruments, techniques and analysis.
- ✗ Laborious, time consuming and expensive technique.
- ✗ Radiological risk to workers.
- ✗ Secondary wastes produced.

B. Radiometric logging

- ✓ Continuous, real-time assessment of vertical soil profiles.
- ✗ Significant challenge to detect α and β emitting radionuclides.
- ✗ Intrinsic limitations of available logging probes.

2. Focus

Magnox Swarf Storage Silo (MSSS) at Sellafield site (UK)

Gamma-ray logging measurements to assess contamination trends near the silo where the greatest activity is present

The probe under development shall **(1)** be compact to fit in the existing array of carbon steel blind-tubes (inner diameter 75 cm); **(2)** resilient to be left in situ; **(3)** hold long-term functionality for high doses (< 1 Gy/h); and **(4)** hold a dual-mode system, that can discern ^{137}Cs and ^{90}Sr.

3. The Concept & Hypothesis

Detection of ionizing radiation present in the ground surrounding a blind-tube.

Direct Detection — YES ✓

^{137}Cs → ^{137m}Ba → γ (0.662 MeV) → ^{137}Ba

Direct Detection — NO ✗

^{90}Sr → β (0.546 MeV) → ^{90}Y → β (2.28 MeV) → ^{90}Zr

Detection of produced bremsstrahlung photons

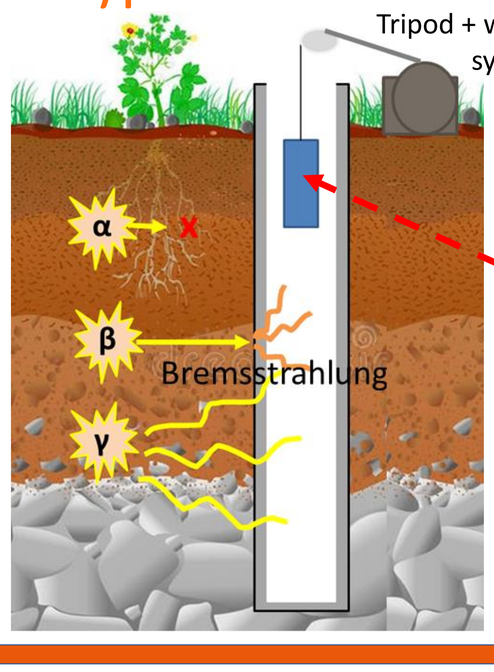

Logging probe prototype and respective components

- **A** — Sensing element: scintillation crystal
- Signal conditioning: PM6660-SiPM + Preamplifier
- **B** — Signal processing: Digitizer MCA
- Visualisation of data

A. Ø10 mm x 9 mm Cerium Bromide ($CeBr_3$) detector

Commercialized by Scionix (Netherlands)

B. TOPAZ-SiPM digital Multi-Channel Analyser

Commercialized by BrightSpec NV

Developed prototype #1

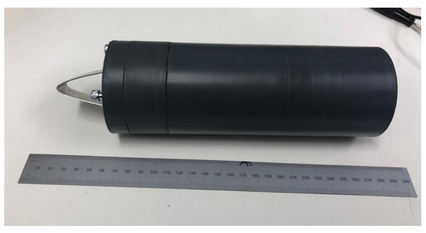

Ø 70 mm

Developed prototype #2

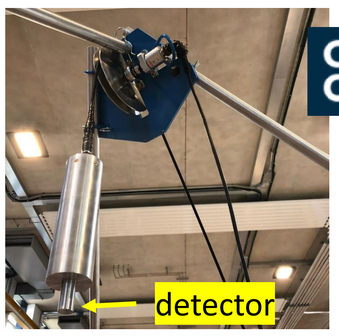

GAME CHANGERS

Hybrid Instruments

ABACUS project

4. Experimental Work

Detector response for contamination via ^{137}Cs and/or ^{90}Sr.

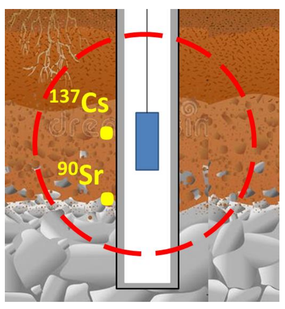

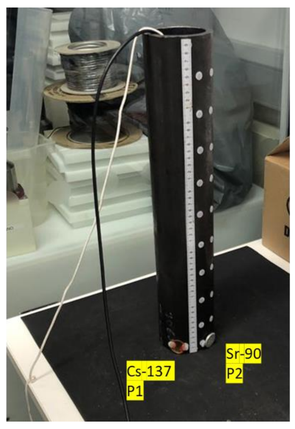

*Spatial source distribution (simplified scenario): disk point sources surrounding the blind-tube but close to its wall.

Obtained Gamma-ray spectra*:

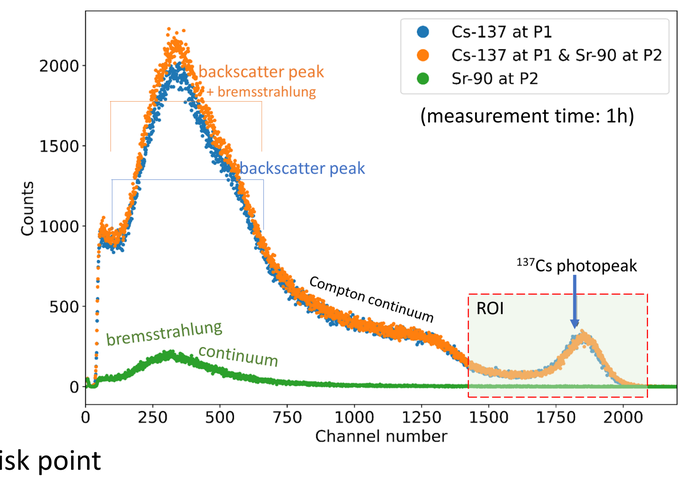

The logging probe may detect ionizing radiation caused by a variety of sources of radiation and output **complex gamma-ray spectra**.
In the present **model** (f_1) the plurality of sources is particularly categorised into a **first source of radiation**, ^{137}Cs the predominant radionuclide, and a **secondary contribution** representative of background radiation + scattered photons + bremsstrahlung photons.

Example of an obtained photopeak ^{137}Cs @ 662 keV and fitting analysis:

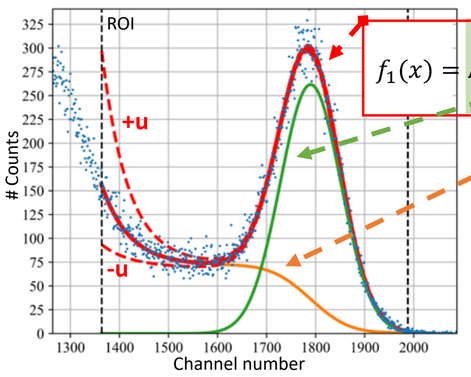

$$f_1(x) = Ae^{\frac{(x-\mu)^2}{2\sigma^2}} + AB\,erfc\left(\frac{x-\mu}{\sigma\sqrt{2}}\right) + ACe^{\frac{x-\mu}{T\sigma}}\,erfc\left(\frac{x-\mu}{\sigma\sqrt{2}} + \frac{1}{T\sqrt{2}}\right) + b$$

$x \equiv$ channel number

✓ The quantity of a principal radionuclide is simply obtained calculating the area under the obtained Gaussian peak.

→ Point-spread analysis of photo-depth spectra

To infer ^{137}Cs photo depth profiles it is crucial to analyse each obtained gamma-ray spectrum individually.
Focus: We're looking for changes in the shape and intensity of successively recorded spectra.

Experimental setup to obtain ^{137}Cs gamma-ray depth profile.

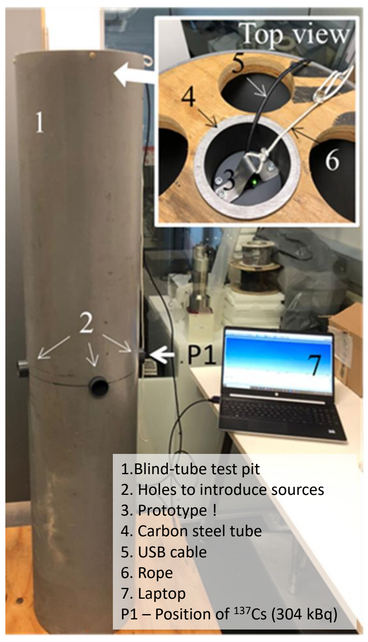

$\text{Depth}_{\text{source}} = 80.2 \pm 0.5$ cm

A. Obtained total gamma-ray depth profile for a ^{137}Cs point source:

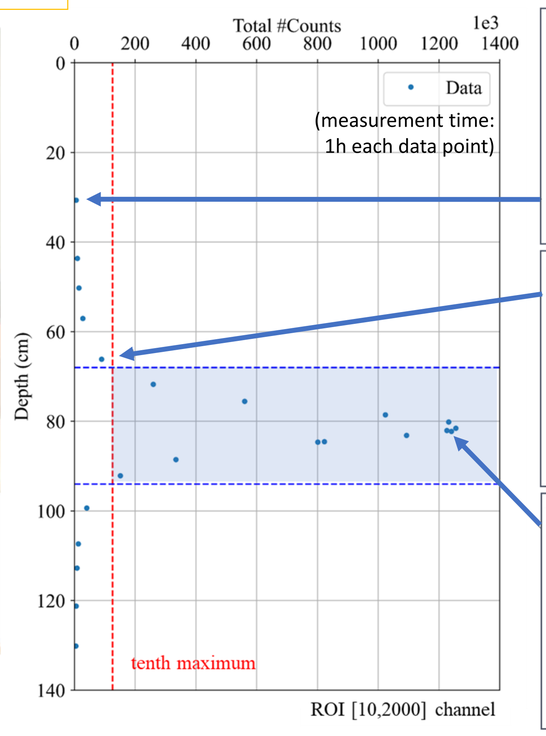

B. Obtained gamma-ray spectra at specific depth positions in the pipe:

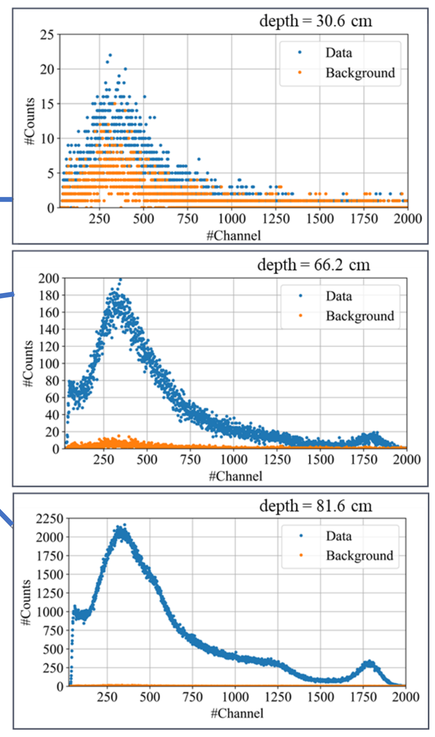

Obtained ^{137}Cs @ 662 keV gamma-ray depth profile:

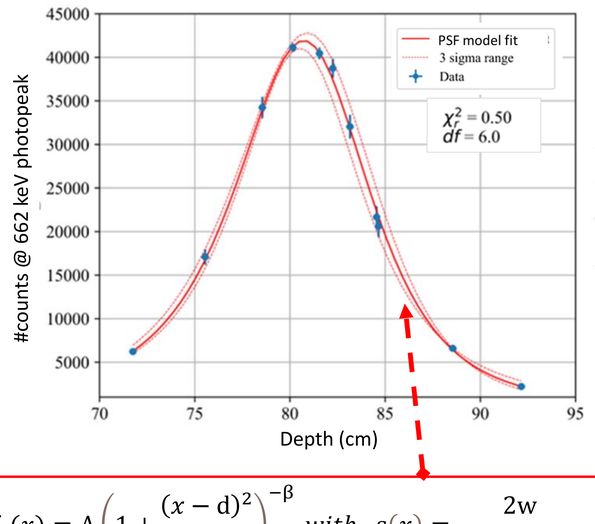

Data was found to be well described mathematically by a continuum point spread function. **Model** (f_2) is a Moffatt function with a skew component.

This function is widely used in the field of stellar astrophysics.

$$f_2(x) = A\left(1 + \frac{(x-d)^2}{s(x)^2}\right)^{-\beta} \quad with \quad s(x) = \frac{2w}{1 + e^{\gamma(x-d)}}$$

$x \equiv$ depth (cm)

$d = 80.7 \pm 0.1$ cm

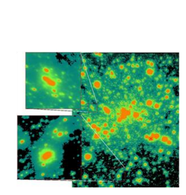

Blurred NIR images of crowded stellar fields

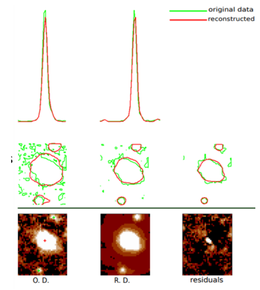

✓ Accurate location of a source of radiation.

The photopeak becomes well defined over the underlying continuum as the detector moves closer to the position of the source.

5. Conclusion & Future Steps

The method enables quantification of ^{137}Cs over a complex continuum background of radiation. It sets the obtained quantitative information of the plurality of spectra in function of depth position and evaluates the change in intensity from one measurement to the next one. And outputs a very accurate location of source in a in-ground blind-tube environment.

SOON → Test of the model for extended source distribution, and when ^{90}Sr is present (peak-to-total analysis).
Deployment of the system in a borehole environment in a contaminated site.

Acknowledgment – This research is supported by NNL and Sellafield Ltd. (UK) via the EPSRC programme TRANSCEND (TRANSformative Science & Engineering for Nuclear Decommissioning), code EP/S01019X/1. M. J. J. acknowledges the support of the Royal Society via a Wolfson Research Merit Award.
Patent – Elísio, S., Joyce, J. M., 29 September 2022, Method and Apparatus for Determining Attributes of a Source of Radiation, P347121GB/CAB.

Seeing with Sound: Advanced characterization for suspension wastes with acoustic backscatter

Joseph Hartley[1*], Timothy Hunter[1], Jeffrey Peakall[2], Richard Bourne[1], Serish Hussain[1].

[1] School of Chemical and Process Engineering, University of Leeds, Leeds, LS2 9JT, UK.
[2] School of Earth and Environment, University of Leeds, Leeds, LS2 9JT, UK.

NUCLEAR ENGINEERING
University of Leeds

[*] Corresponding Author: pmjha@leeds.ac.uk

Background & Introduction

Use of acoustic backscatter to characterise high concentration sediments in the near-field, and characterisation of bi-disperse systems is not yet fully understood.

Application of these techniques is being introduced to monitor the PSDs of legacy nuclear waste sludge which are currently undergoing processing and disposal.

The processing utilises polymeric behaviour modifiers which aid settling, but are shear dependent.

As such Machine Learning (ML) will help to automate and improve the analysis of the backscatter data so the concentration and PSD can be characterised relatively easily, and the changes of these measurements can be tracked through time with varying shear.

Research Aims

- Size Characterisation of virgin vs. sieved size fractions and bimodal size fraction mixtures of spherical glass particles.
- Development of Machine Learning code to characterise size and concentration of spherical glass particles.
- Application of aforementioned research to flocculated systems.

Fig 2 – Python logo (Wikipedia, 2021).

Fig 3 – Schematic of calibration rig used in this project for collecting acoustic data, modified from Hussain et al. (2020).

Material & Methods

Fig 1 – PSD of bi-modally distributed small and large, data gathered using a Malvern Mastersizer 3000. Spherical silica glass beads of different sizes, d50=41µm and d50=81µm, were mixed at 25:75, 50:50, and 75:25 wt.% and tested over a concentration range 14 to 68g/L.

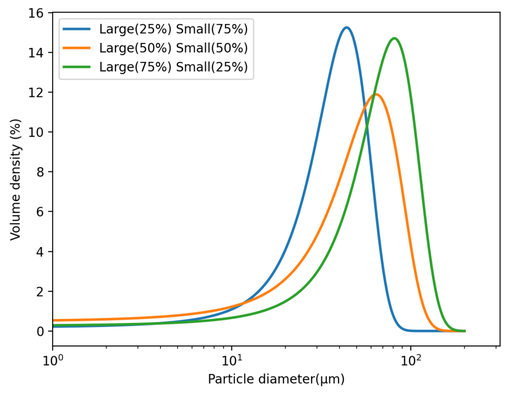

Acoustic data was collected using *in situ* probes with the UVP-DUO on homogenised suspensions.

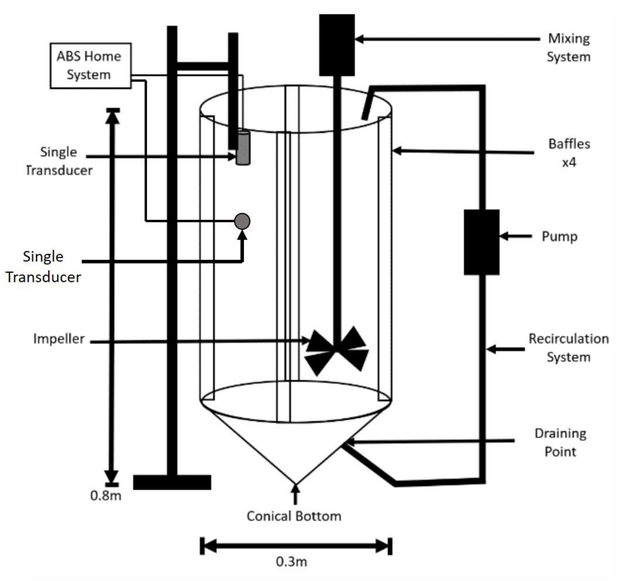

Data were analysed in Python scripts and the concentration independent sediment attenuation coefficients (SAC) for all mixes at 2MHz and 4MHz were calculated using the G-function method outlined in Bux et al. (2019).

Comparison of these measured SACs against values calculated from the acoustic models in literature, which incorporate attenuation losses from both viscous elastic and scattering mechanisms, are plotted below.

Results & Discussion

Fig 1 – Backscatter G-function vs. distance from transducer, at 2MHz (*left*), and 4MHz (*right*); for 25:75 (*top*), and 50:50 (*bottom*) wt.% mixes of large : small glass. Vertical black lines show where the gradient of each plot was taken.

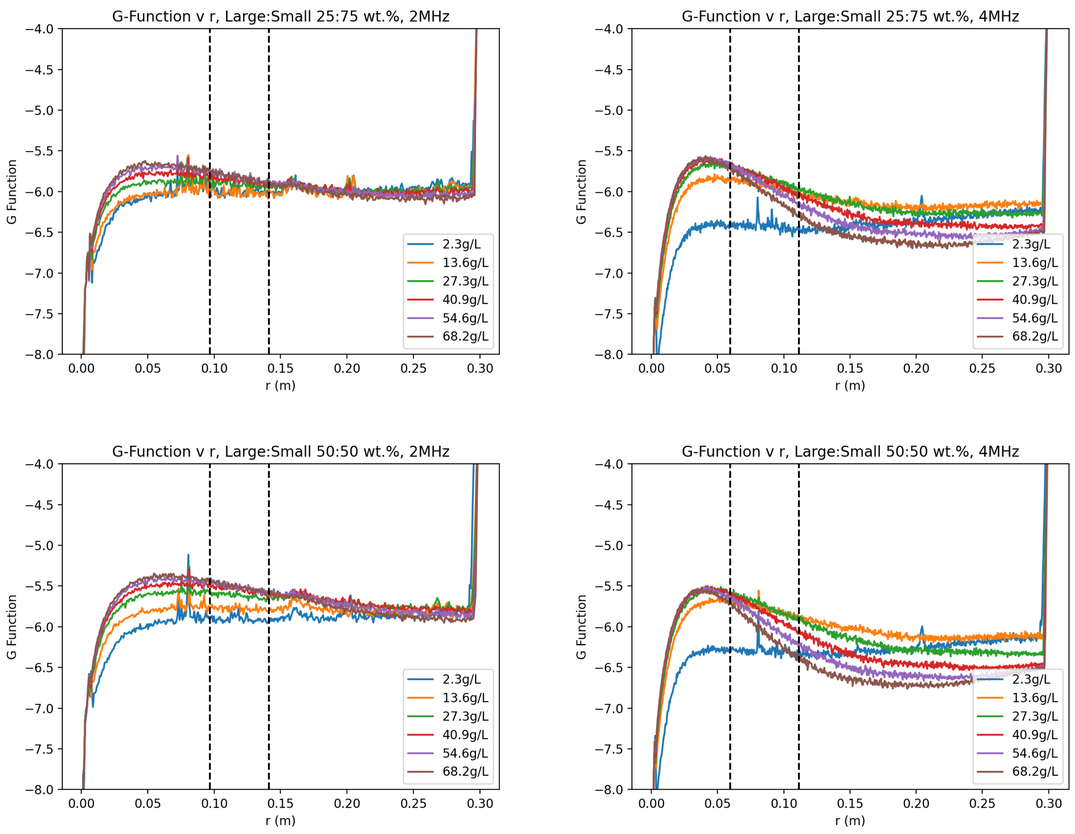

Fig 5 – dG\dr (gradient from G-function vs. distance from transducer in Fig4) vs. concentration for all data collected.

The 4MHz signal for the large glass highlights the limits of the UVP transducer as the points bottom out, thus a gradient is only taken from the first three points.

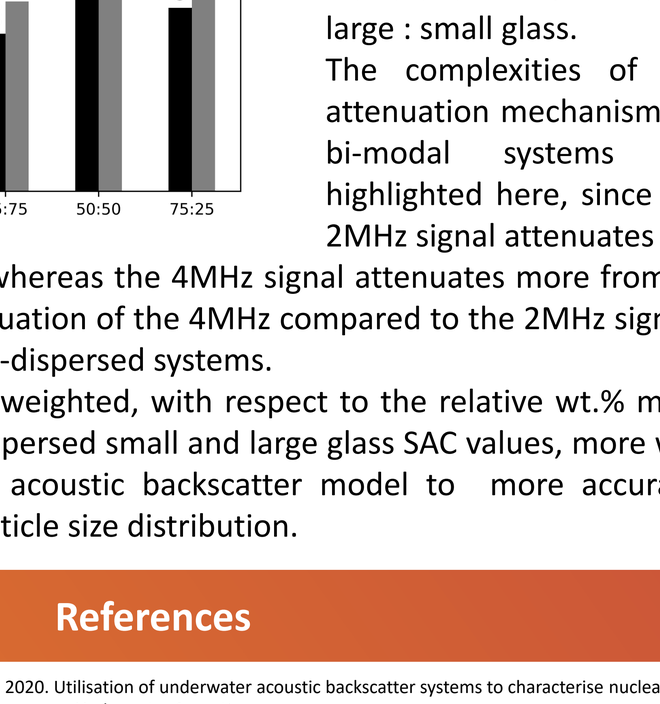

Fig 6 – Concentration independent SAC for all systems in comparison to calculated values from the model for scattering losses (Urick, 1948), ratios on the x-axis show wt.% mixes of large : small glass.

The complexities of the attenuation mechanisms in bi-modal systems are highlighted here, since the 2MHz signal attenuates more from the small glass, whereas the 4MHz signal attenuates more from the larger glass, the higher attenuation of the 4MHz compared to the 2MHz signal is still apparent from the mono-dispersed systems.

Calculated values are linear weighted, with respect to the relative wt.% mixes, summations of the mono-dispersed small and large glass SAC values, more work is required to develop the acoustic backscatter model to more accurately incorporate the bi-modal particle size distribution.

Conclusions & Further work

- More work needed to match measured and calculated SACs of bi-modal systems.
- SACs larger for 4MHz than 2MHz, but more complicated when comparing between bi-modal mixes.
- Same systems were tested using Aquascat ABS, data to be analysed.
- ➢ Develop the acoustic backscatter model to incorporate bi-modal particle size distribution coefficient/factor.
- ➢ Gather data on number distributed bi-modal mixes in the same way.
- ➢ Investigate the effect of radiation on ultrasonic acoustic probes.
- ➢ Development of ML code package for determination of PSD, from acoustic backscatter data.

References

Hussain, S.T., Hunter, T.N., Peakall, J. and Barnes, M. 2020. Utilisation of underwater acoustic backscatter systems to characterise nuclear waste suspensions remotely. In: *International Conference on Underwater Acoustics*.

Bux, J., Peakall, J., Rice, H.P., Manga, M.S., Biggs, S. and Hunter, T.N. 2019. Measurement and density normalisation of acoustic attenuation and backscattering constants of arbitrary suspensions within the Rayleigh scattering regime. *Applied Acoustics.***146**, pp.9-22.

Urick, R.J. 1948. The absorption of sound in suspensions of irregular particles. *The Journal of the Acoustical Society of America.***20**(3), pp.283-289.

Wikipedia. 2021. *Python (programming language).*[Online]. [Accessed 07/11/21]. Available from: https://en.wikipedia.org/wiki/Python_(programming_language)

Electrokinetic remediation of difficult-to-measure radionuclides at nuclear sites

Shaun D. Hemming, Frances M. Burrell, Ian T. Burke, Richard I. Marsh, James Graham, Phil E. Warwick and Andy B. Cundy

S.D.Hemming@soton.ac.uk

National Oceanography Centre, Univ. Southampton, European Way, Southampton, UK SO14 3ZH

What is Electrokinetic Remediation (EKR)?

- Clean-up of the UK's nuclear legacy is estimated at ~ £200 billion over 100 years
- There is an urgent need to reduce decommissioning costs - could new approaches to remediation help?
- Technique must work in soils, sands, concretes, cements, groundwater, *etc.*, AND be site-scalable, cheap, energy efficient and sustainable

EKR involves decontamination by electrocution, concentrating pollutants within cell or at electrodes. It is an adaptable and low-energy waste minimisation technique

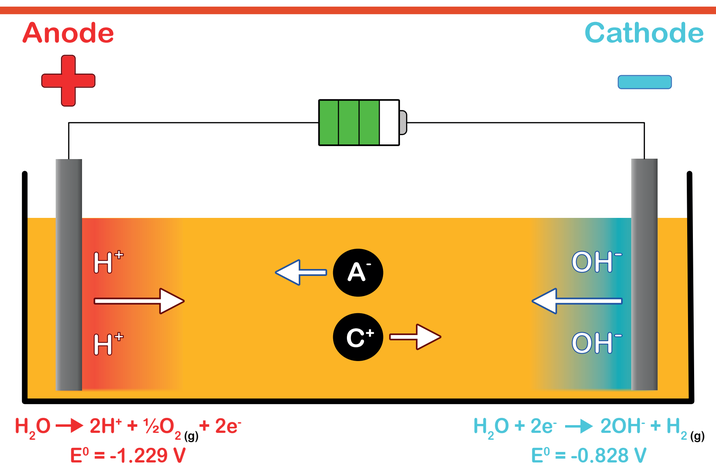

Figure 1: A typical electrokinetic cell. C^+ are cations and A^- are anions

Cements - Ongoing Work

- Collaborative work with Ian Burke (University of Leeds) and the NNUF-EXACT facility (Southampton) into whether electrokinetics can remediate cement containing ^{236}U, ^{137}Cs, ^{129}I, ^{90}Sr and ^{3}H
- Cement was chosen instead of concrete to simplify the system. Consequently, only cement and water were added, in a 2:1 ratio
- Cement cores were contaminated in 2 different ways:
  - — Homogeneous Set - radionuclides were added as the cement and water were mixed (RNs are homogeneously distributed throughout core, simulating concrete biosheilding)
  - — Soaking Set - cores were left to harden (known as curing) for 28 days and, afterwards, placed in a bath containing radionuclides (RNs are bound to the surface or near-surface, simulating storage pond concretes)
- Cores have been treated and are currently being analysed. Preliminary data from electrolytes (below) shows that overall mobility differed between each radionuclide, as well as a strong indication that a greater degree of mobilisation occurs in the Soaking Set compared to the Homogeneous Set

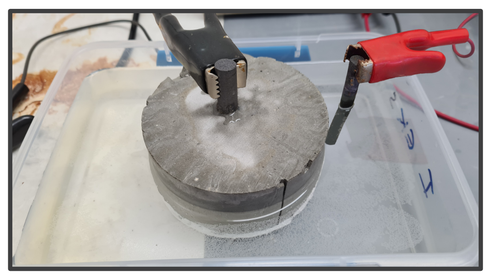

*Figure 2: **Above** - trial cement core undergoing electrokinetic treatment.*

***Below** - graphs showing the proportion of radionuclides in cement cores that migrated and/or diffused into the electrolytes during the 6 week treatment period.*

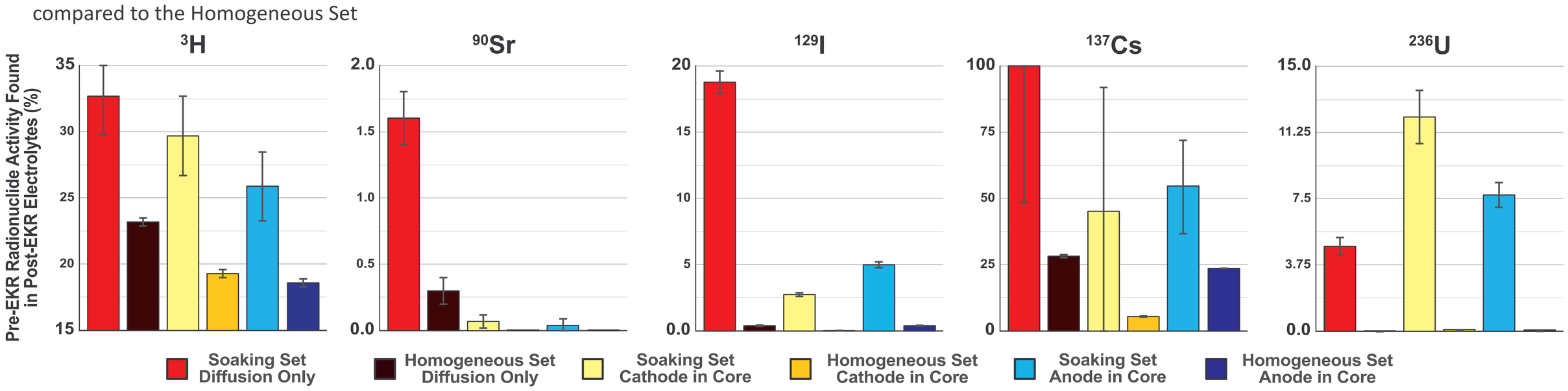

Groundwaters - Ongoing Work

- Investigation into the application of electrokinetics for 54 hour remediation of stable Sr, I and Re (as an analogue for Tc) in Sellafield groundwater simulant
- 3 types of cell were created:
  - — sand only (simplified setup)
  - — 80% sand and 20% clay, homogeneously mix (more representative of Sellafield subsurface)
  - — sand with 2 biochar barriers (charcoal derived from sewage sludge; proof of concept for a system that utilises both EKR and permeable reactive barriers (PRBs)
- EKR impact is most notable in middle wells, where concentrations of Sr, I and Re decrease over time
- The percentage of post-EKR target nuclide concentrations is, on average, 10% higher in the EKR cells compared to the control cells. This implies EKR is migrating ions away from the centre quicker than by diffusion alone

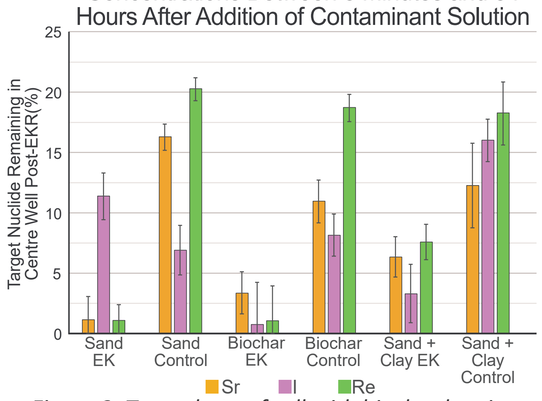

*Figure 3: **Top** - photo of cell with biochar barriers. **Bottom** - Graph to show concentration reductions of Sr, I and Re in the middle well of each cell*

Sediment Core - Upcoming Work

- Evaluation of whether electrokinetics can migrate the radionuclides present in a 55 cm sediment core from the Ravenglass saltmarsh (~9 km south east of Sellafield)
- Sellafield discharges into the Irish Sea have accumulated in the saltmarsh
- Historical discharges are buried over time by new sediment, creating a discharge profile in the core
- Radionuclides may have been remobilised over time due to changes in conditions
- Itrax XRF scan shows stable element composition throughout the core. Key elements are:
  - — S indicates whether the sulphidic zone of respiration has been reached
  - — Mn and Fe mark sub-oxic zone of respiration
- Radionuclide analysis will follow soon

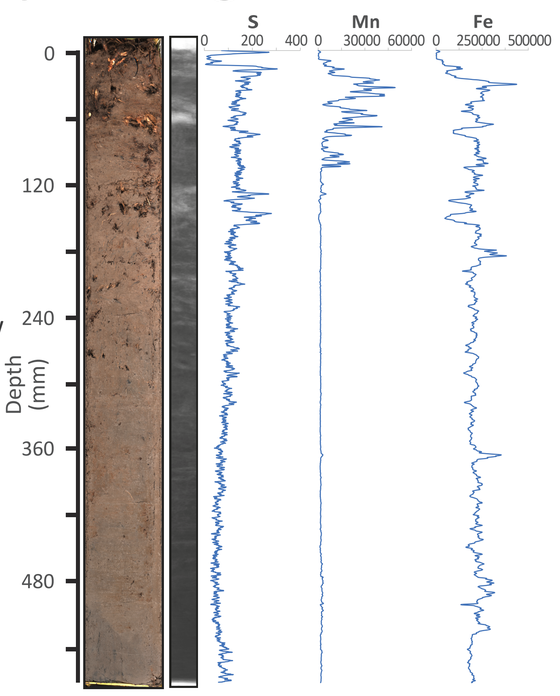

Figure 4: Optical image, radiograph and Itrax XRF scan of key stable elements in the Ravenglass sediment core before EKR treatment

Acknowledgements: GAU Radioanalytical; NERC, INSPIRE DTP and TRANSCEND consortium project (EPSRC grant number EP/S01019X/1) for funding; the British Ocean Sediment Core Research Facility (BOSCORF) for supporting XRF core scanning; the National Nuclear User Facility EXACT laboratory and team, via the UK EPSRC (grant EP/T011548/1), for support with cements work.

Transformative Science and Engineering for Nuclear Decommissioning

transcendconsortium.org

Development of Composite Zeolites for Remediation of Nuclear Wastewaters

James Reed[a*], Phoebe Allan[a] Thomas Carey[b] and Joseph Hriljac[c]

[a]School of Chemistry, University of Birmingham, Edgbaston, Birmingham, UK.
[b]National Nuclear Laboratory, Chadwick House, Birchwood, Warrington, UK.
[c]Diamond Light Source Ltd., Harwell Science and Innovation Campus, Didcot, UK.

JLR552@student.bham.ac.uk

Background

- Decommissioning at the Sellafield site is expected to last ~100 years and cost 10's billions of pounds to the UK taxpayer – it therefore needs to be efficient to minimize cost and environmental impact.[1]
- Key challenge is removal of Cs-137 and Sr-90 from aqueous waste streams.
- The anionic framework, uniform channels, resistance to radiation and physical durability make zeolites ideal for this purpose.[1]
- A clinoptiliolite (clino) zeolite, sourced from Mud Hills, California, has been utilized on site for >30 years due to its high affinity for both cesium and strontium – however, supply is only expected to last into the 2030s.
- Other clinoptilolites have been shown to not match the performance of material sourced from Mud Hills, particularly its ability to capture strontium.[1]
- Innovative materials capable of dual Cs and Sr uptake must therefore be sourced to help us meet future decontamination efforts.
- **This work looks at the generation of composite zeolites through partial transformations to the atomic framework structure and subsequent use for Cs and Sr encapsulation (Figure 1).**

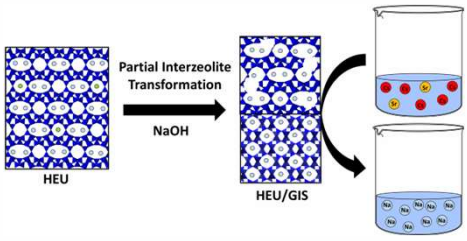

Figure 1: Remediation of aqueous nuclear decommissioning waste using a zeolite composite.

Generation of Zeolite Composites

- Chemical modification of natural zeolite materials was achieved via hydrothermal treatment with NaOH.
- Zeoclere clinoptilolite (HEU topology) and mordenite zeolite (MOR topology) underwent transformation into Na-P (GIS topology).
- Degree of transformation controlled through the manipulation of NaOH concentration (Figure 2).
- High level of control exhibited: optimised blend of phases can be prepared.
- Starting materials (clino and mordenite) good for caesium encapsulation due to larger 10/12 ring channels and higher Si/Al (~4.5).
- New Na-P phase better for strontium due to smaller 8 ring channels and more aluminium enriched frameworks (Si/Al ~2.5).
- Composites good dual-uptake materials in principle.
- Control over composite phases gives potential to 'tune' material to a given waste stream e.g more Na-P phase developed to remediate high strontium feeds.

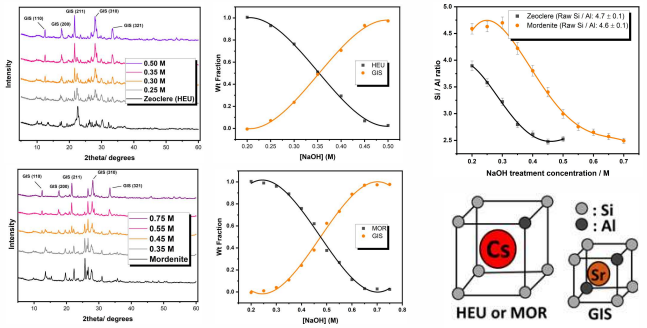

Figure 2: PXRD patterns of NaOH treated zeolites (left). Weight fractions of parent and resultant phase as a function of [NaOH] (centre). Si/Al ratio of treated zeolites (top right). Preferential encapsulation of cesium and strontium cations in a variety of zeolite frameworks (bottom right).

Cs and Sr uptake experiments

Inactive batch testing in K/Ca matrix (Figure 3)

- 10 ppm Cs/Sr, 50 ppm K/Ca.
- Strontium uptake increases at expense of caesium uptake as transformation proceeds.
- Composites show improvement in removal rates (good dual Cs/Sr exchange materials).

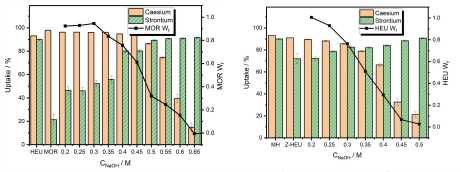

Figure 3: Cesium and strontium batch uptake data for materials derived from mordenite MOR (left) and Zeoclere HEU (right).

Active Flow testing (Figure 4)

- Using RIX method developed by NNL with no competing cations (0.017 ppm Cs-137, 0.0005 ppm Sr-90).
- Composites displayed enhanced Cs-137 removal rates.
- A drastic improvement in Sr-90 removal rate was also observed.
- **50:50 composites generated from natural mordenite and Zeoclere clinoptilolite outperformed industry-used Mud Hills clinoptilolite.**

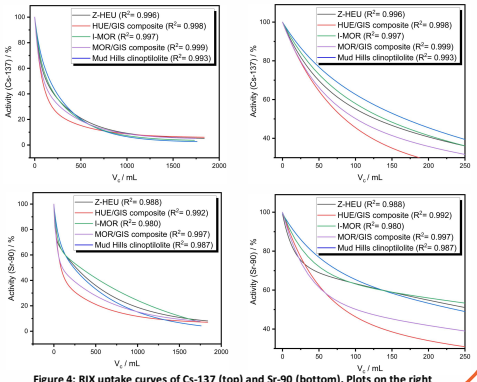

Figure 4: RIX uptake curves of Cs-137 (top) and Sr-90 (bottom). Plots on the right focus on the first 250 mL column throughput.

Macroscale mechanism of transformation (determined with data from DIAD, DLS)

- Granular materials derived form mordenite were selected for further characterisation at K11 DIAD, Diamond Light source[2].
- DIAD facilitates quasi-simultaneous imaging and micro-diffraction. This allows for the collection of diffraction patterns at regions of interest (e.g the edge of the granule).
- Cross-sectional tomography imaging (Figure 5) revealed formation of an outer shell during interzeolite transformation.
- Diffraction data confirmed this outer shell to be zeolite P (GIS).
- Interior then recrystalises into zeolite P until transformation is complete.
- Core-shell model also supported by diffraction tomography (Figure 5, bottom centre).

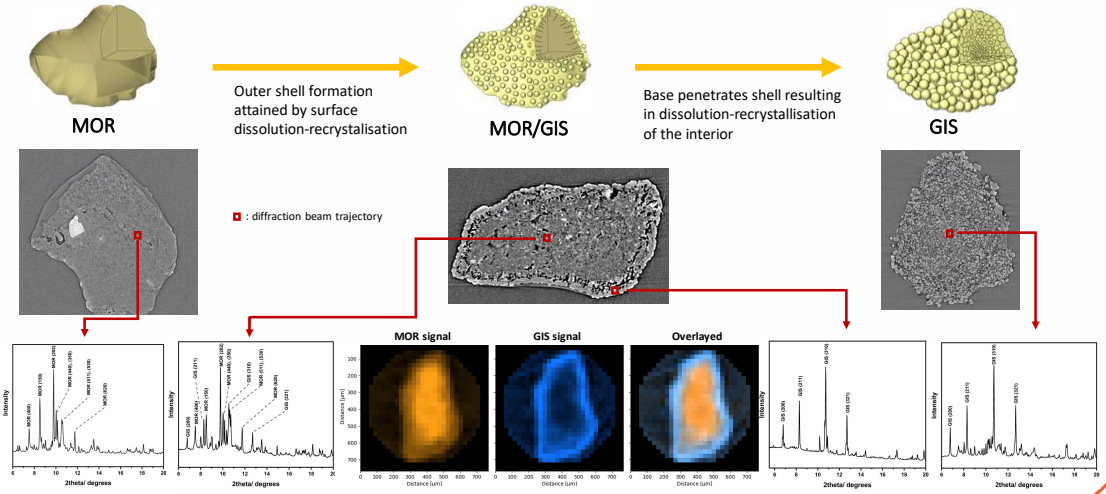

Figure 5: Schematic displaying proposed mechanism of transformation (top). Computed tomography images elucidating the mechanism of transformation (centre row). Local diffraction patterns of selected regions (λ = 0.0597 nm, bottom left and right). Spatially resolved diffraction tomography of composite particle (bottom centre). MOR and GIS phase intensities determined through integration of MOR (620) and GIS (200) reflection peaks.

References

1. Dyer, A. *et al.* The use of columns of the zeolite clinoptilolite in the remediation of aqueous nuclear waste streams. *Journal of Radioanalytical and Nuclear Chemistry* **318**, 2473-2491 (2018). https://doi.org:10.1007/s10967-018-6329-8
2. Reinhard, C. *et al.* Beamline K11 DIAD: a new instrument for dual imaging and diffraction at Diamond Light Source. *Journal of Synchrotron Radiation* **28**, 1985-1995 (2021). https://doi.org:10.1107/s1600577521009875

Acknowledgements

- PhD supported by Sellafield Ltd and National Nuclear Laboratory as part of the TRANSCEND consortium.
- Active work was funded by Nuclear Decommissioning Authority and National Nuclear Laboratory.
- Tomography and local diffraction data collected at Diamond Light Source with help from Andrew James.

Transformative Science and Engineering for Nuclear Decommissioning

transcendconsortium.org

In-situ Corrosion Tests of Stress Corrosion Cracking using a Novel Small Punch Test Design

K. Yuan[1]*, R. Clark[2], M. Mostafavi[1]

[1]Department of Mechanical Engineering, University of Bristol, BS8 1TR
[2]National Nuclear Laboratory, 102B Stonehouse Park, Stonehouse, Gloucestershire, GL10 3UT

*k.yuan@bristol.ac.uk

Introduction

Aim

To develop a new small punch test (SPT) setup for spent AGR cladding with surrogate material (thermally sensitised 304 stainless steel) that can initiate SCC (stress corrosion cracking) of stainless steel in a short period time for DIC (Digital image correlation) observation.

Two DIC pattern methods are compared for the special corrosive environment.

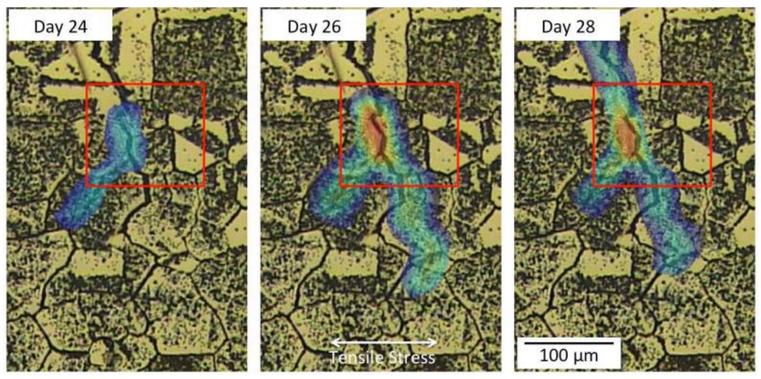

Fig. 1. DIC strain mapping of the development of a stress corrosion crack*

Background

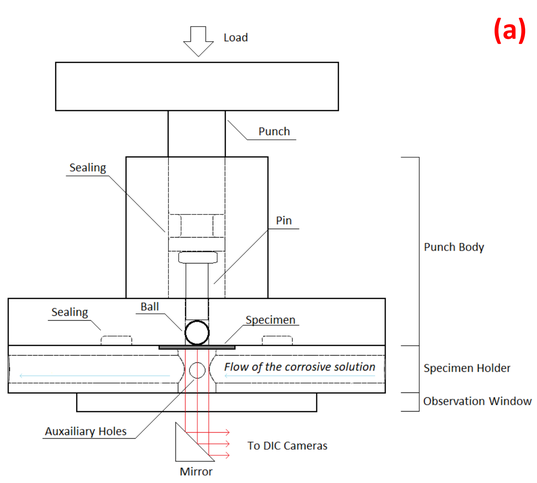

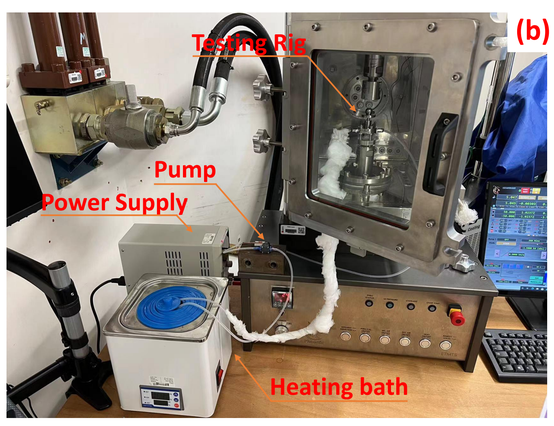

Fig. 2. (a) Schematic of the new SPT design and (b) the loop system

A SPT setup has been designed and built to allow the SPT held at a constant load while a loop of heated corrosive solution (1000 ppm sodium thiosulphate) is circulated around the sample for accelerating the initiation of SCC. A mirror is also placed below the sample to allow observing with a Lavision stereo micro DIC, which has a magnification from x2.4 to x30.

A trial test was conducted without DIC to prove that the new setup can successfully initiate SCC. A 1000 ppm sodium at 60 °C was circulated in the loop, and a constant load of 1.5 kN was applied. After 113 hours, SCCs were observed on the surface of the SPT sample.

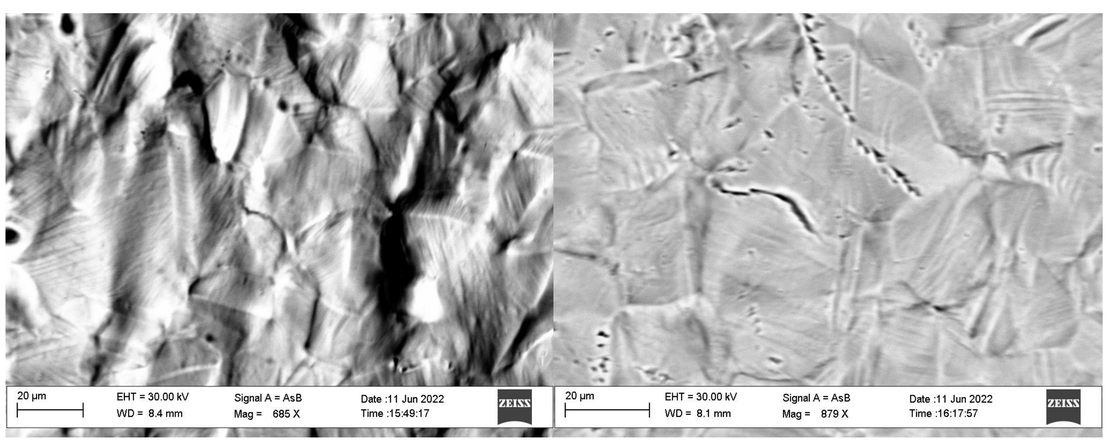

Fig. 3. Stress corrosion cracks observed on the small punch test sample

Pattern Preparation

Both the samples were electro polished in 92% acetic acid and 8% perchloric acid at 42v for 60s beforehand to give a fine surface.

- Painted: black dots painted by an airbrush with high temperature primer
- Electro etched: in a 92% acetic acid and 8% perchloric acid solution at 13v for 20s*

Fig.4. painted (left) and etched (right) SPT samples

Comparisons

To compare the correlation quality of two patterns, rigid body movement test have been done by moving the micro DIC cameras horizontally by 100 µm. Due to the corrosive environment, two tensile samples, which were prepared in the same two ways, were loaded and place in the same corrosive condition for 105 hours to find out the effect on the patterns.

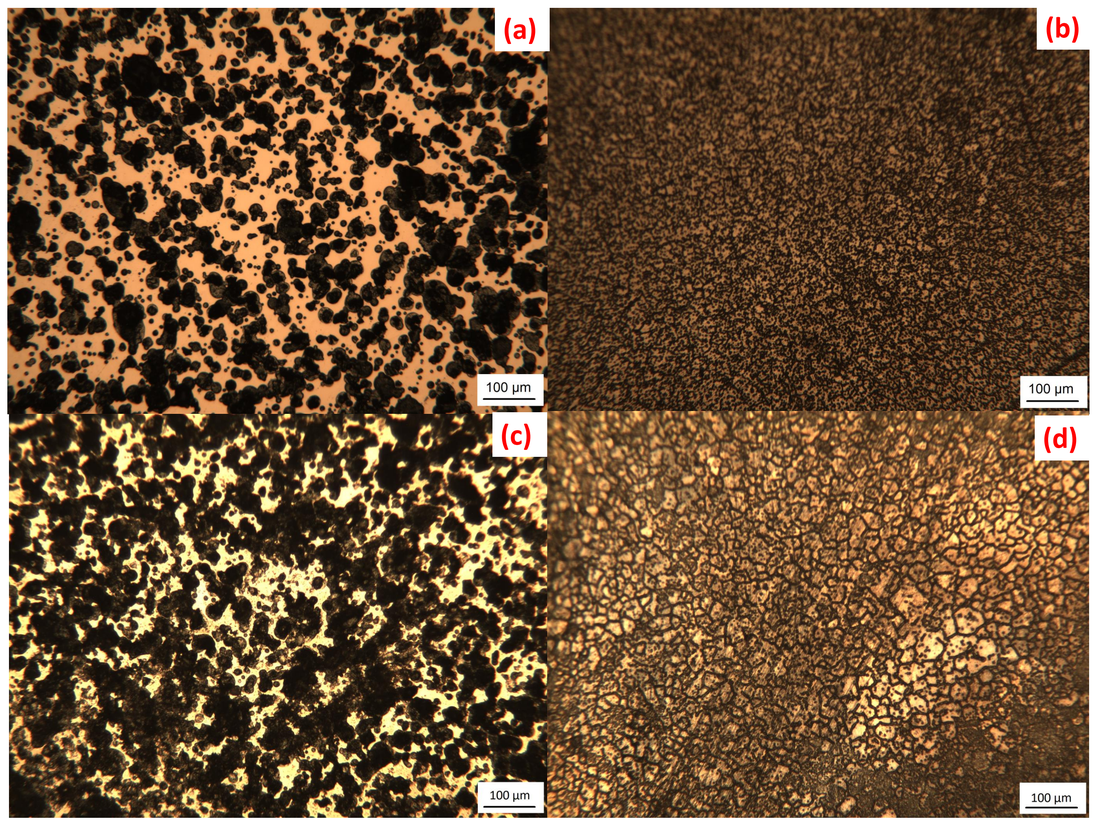

Fig. 5. (a) painted surface before corrosion, (b) etched surface before corrosion; (c) painted surface post corrosion, (d) etched surface post corrosion.

The paint spots are much larger than the etched features. After corrosion tests, the painted surface is heavily corroded by pitting, but the etched surface remains intact.

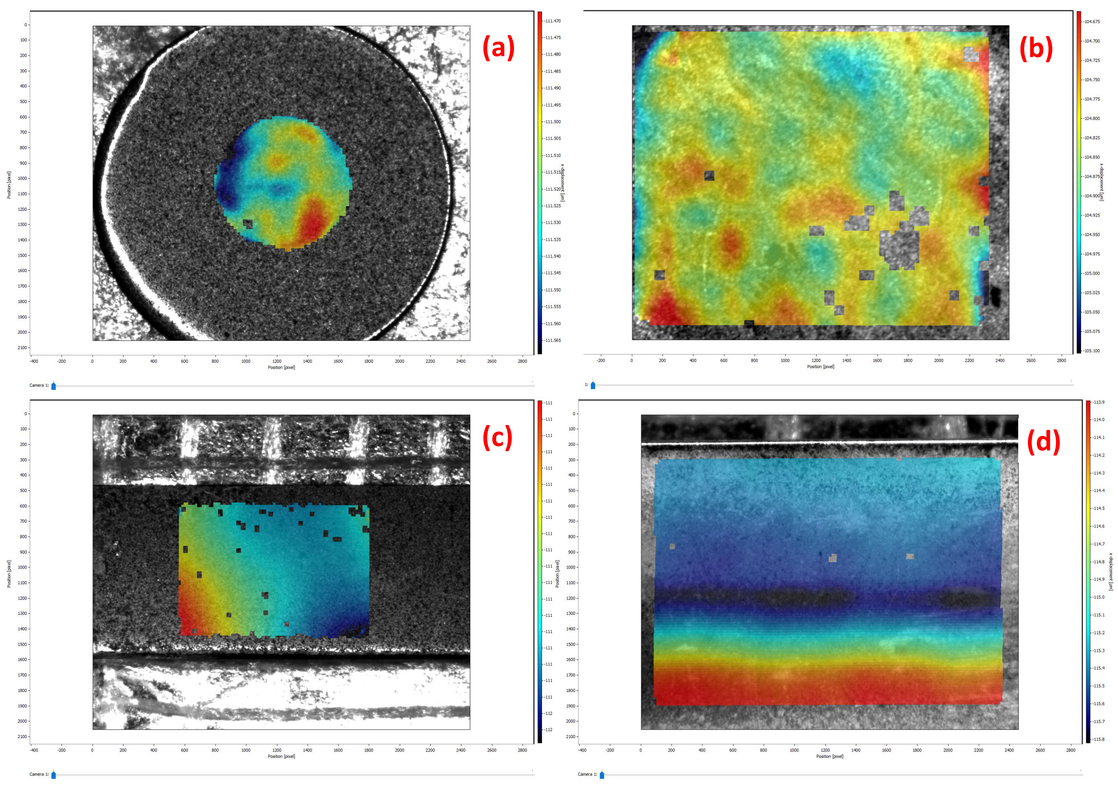

Fig. 6. Correlation of (a) painted surface before corrosion (x10), (b) etched surface before corrosion (x20); (c) painted surface post corrosion(x10), (d) etched surface post corrosion (x20).

The rigid body movement tests showed that the quality of the painted surface deteriorated after the corrosion tests as many missing spots are showing on the surface. The error for the painted sample increased from 9 µs to 84 µs, but the error of the etch sample only increased from 39 µs to 85 µs.

Conclusions

Two patterns for DIC under the corrosive condition has been compared, and etching will be used as the preferred method for patterning in the DIC of SPT. Similar correlation will be done in the SPT to see the effect of fluid on DIC.

References

*Stratulat, A., Duff, J., Marrow, J. (2014), Grain boundary structure and intergranular stress corrosion crack initiation in high temperature water of a thermally sensitised austenitic stainless steel, observed in situ, *Corrosion Science*, 85, 428-435

Electrokinetic in-situ decontamination of entrained radioactivity within a concrete matrix

T. McCarthy [a b], C. Boxall [a], M. Joyce [a], A. Banford [b]

[a] Department of Engineering, Lancaster University

[b] National Nuclear Laboratory, Workington Laboratory, CA14 3YQ

Introduction

Concrete is ubiquitous on nuclear sites as construction (*Figure 1*), shielding and plant/pond material and may be readily contaminated by exposure to $\alpha/\beta/\gamma$ emitters.

There are four common techniques used for the decontamination of intact concrete structures:

- Scarifying
- Abrasive blasting
- High-pressure liquid jetting
- Laser ablation

However, each of these have limitations and yield secondary waste.

This project will investigate the efficacy of a decontamination technique previously used to remediate contaminated soils named Electrokinetic remediation [1].

Electrokinetic remediation is the application of an electric field as a means of migrating contaminants in a heterogeneous solution through the porous network present within the concrete matrix.

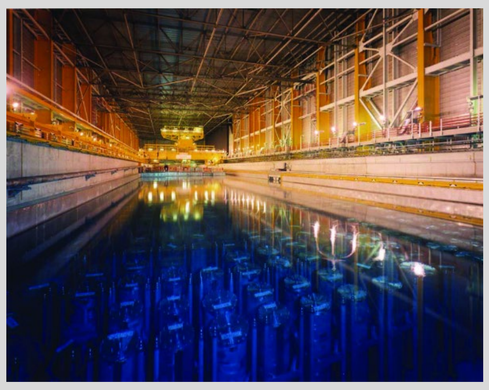

***Figure 1**: Concrete storage pond at Sellafield, UK [2]*

Project Aims

There are three main aims of the project:

1. A survey of the properties of commercial concrete compositions, inc. their porosity, surface pH & crystal structure to establish a database of concrete chemistries.
2. Determine analogue adsorption into the concrete microstructure through use of analytical techniques.
3. Utilisation of electrokinetic methodologies developed by Parker et al. to understand the factors influencing the efficiency of decontamination (*Figures 2 and 3*) [3].

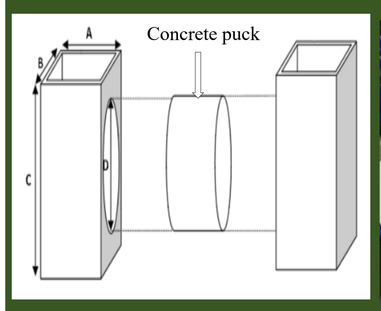

***Figure 2**: The 3D CAD model of the phantom designed by Parker [3] with the following internal dimensions as indicated: A) 55 mm, B) 130 mm, C) 145 mm, D) 110 mm.* [3-7]

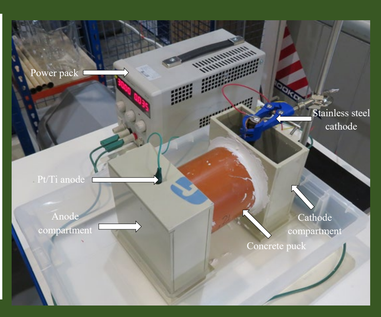

***Figure 3**: Analytical phantom, designed by Parker [3-7]. Platinum sensing electrodes have been omitted for clarity*

Electrokinetic Technique

- Concrete was fabricated to a composition of 1:1.5:0 (Ordinary Portland Cement (OPC), siliceous sand and aggregate).
- For these initial studies, aggregates were omitted from the mix in order to:
  - Limit the number of variables studied.
  - Yield more homogeneous samples.
- Concrete samples were cut into 25-, 35- and 65-mm sections from a 150 mm long concrete cylinder of 110 mm in diameter.
- The electrokinetic apparatus was running continuously at 30 V and 35 mA.
- A stainless-steel electrode was used as the cathode and a Pt/Ti mesh as the anode.
- The cathode and anode compartments were filled with 1.38 L of doubly deionized water to remove the K^+ ions entrained within the concrete samples.

Effects on Concrete

Key observations of ICP-MS (*Figure 4*):

- Concentration of K^+ ions in the compartments for the first days are determined on the diffusion of K^+ ions.
- After 10 days, effect of electromigration can be seen through the concrete sample.
- One compartment was monitored with the assumption of diffusion being the dominant transport mechanism.

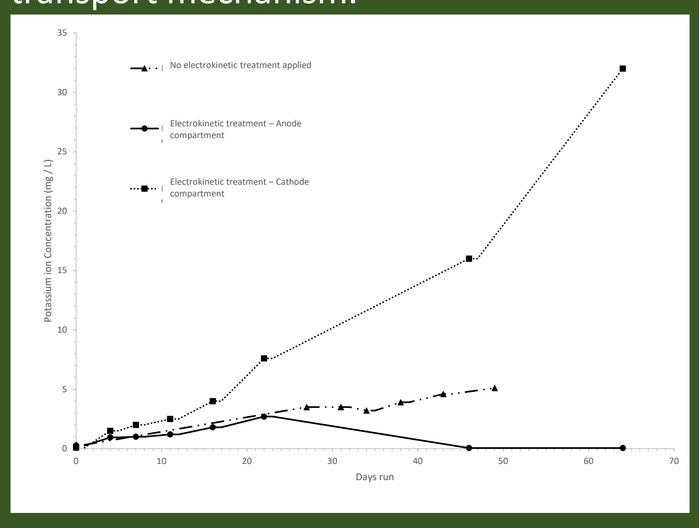

***Figure 4**: ICP-MS results of the change in potassium ion concentration in the cathode and anode compartment under electrokinetic treatment compared to no electrokinetic treatment is applied where the only ion transport mechanism is diffusion.*

Figure 5 shows the pH vs. t data where there is no application of electrokinetic technique that can be attributed to the movement of ions through passive diffusion.

- Over time, ions will not move between compartments as there is no concentration gradient.
- The acidic front generated in the anode compartment can cause corrosion to the concrete surface.

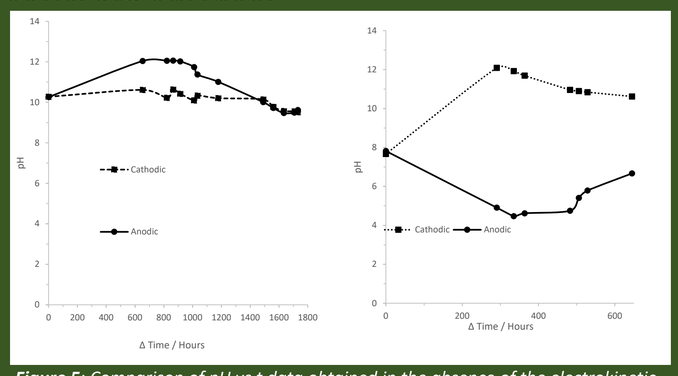

***Figure 5**: Comparison of pH vs t data obtained in the absence of the electrokinetic driving voltage (5a) vs. that obtained in its presence (5b).*

Gamma Irradiation Study

- This investigation seeks to determine the effects of prolonged γ-ray exposure from wet samples [8-10]. This will:
  - Be comparable to dose levels experienced by concrete at the FGMSP.
  - Give an indication of the rate of uptake into radiation-damaged concrete [3-7].
- Concrete samples were run through the electrokinetic process to remove any removable ions from the concrete samples.
- The samples were crushed and dried at 50°C for 3 days to remove any excess water
- 64, 1 g cubes of concrete were soaked in 10 ml of 0.1M CsCl solution for 1 week under ambient conditions, purged under argon.
- Samples were irradiated under a ^{60}Co γ-ray source for 30 hours and were exposed to a total dose in the range 0.061 – 0.455 MGy.
- $[Cs^+]$ was shown to decrease at higher total dose rates, plateauing after a dose of ~0.195 MGy, indicating that the concrete samples had become saturated with $[Cs^+]$ after 30 hours of irradiating.

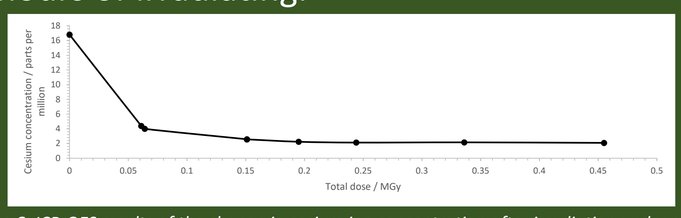

***Figure 6**: ICP-OES results of the change in cesium ion concentration after irradiation under a ^{60}Co gamma-ray source for 30 hours*

Conclusions

- The electrokinetic technique at 30 V and 35 mA was found to be more effective than through solely passive diffusion for the removal of K^+ ions.
- Irradiation causes an increased rate at which Cs is absorbed into concrete samples.
- Solution $[Cs^+]$ decrease plateaus after a total dose of ~0.195 MGy to samples.

Future Work

- Characterise irradiated samples to understand the interaction of Cs on the concrete microstructure.
- Irradiate samples whilst conducting the electrokinetic process to determine the effects of radiolysis.
- Repeating experimental techniques to determine the origin point of the plateau.

References

[1] K.R. Reddy, C.Y. Xu, S. Chinthamreddy, Assessment of electrokinetic removal of heavy metals from soils by sequential extraction analysis., J. Hazard. Mater. 84 (2001) 279–296

[2] "Engineering a transformation at Sellafield" [Online] Available: https://www.neimagazine.com/features/featureengineering-a-transformation-at-sellafield-6231360/featureengineering-a-transformation-at-sellafield-6231360-493914.html [Accessed 27.01.2022].

[3] A. J. Parker, *In-situ* electrokinetic remediation for the reduction of surface-derived dose from radioactive concrete, PhD Thesis, Lancaster University, 2014.

[4] A.J. Parker, M.J. Joyce, C. Boxall, A radioanalytical phantom for assessing the efficacy of electrokinetic decontamination of entrained radioactivity within concrete media, J. Radioanal. Nucl. Chem. 300 (2014) 769–777.

[5] A.J. Parker, J.W. Dickinson, C. Boxall, M.J. Joyce, An electrochemical method for the production of graphite oxide, Electrochem. Soc. Trans. 54 (2013) 23–32.

[6] A.J. Parker, C. Boxall, M.J. Joyce, P. Schotanus, A thalium-doped sodium iodide well counter for radioactive tracer applications with naturally-abundant 40K, Nucl. Instruments Methods Phys. Res. Sect. A Accel. Spectrometers, Detect. Assoc. Equip. 722 (2013) 5–10.

[7] A.J. Parker, C. Boxall, M.J. Joyce, A method for the replacement of 137Cs with 40K as a non-hazardous radioactive tracer for open-source decommissioning research applications, J. Radioanal. Nucl. Chem. 295 (2013) 797-802.

[8] Mirhosseini, S.; Polak, M.A.; Pandey, M., Nuclear radiation effect on the behaviour of reinforced concrete elements, *Nuc. Eng. Des.* 269 (2014) 57-65.

[9] O. Kontani, Y. Ichikawa, A. Ishizawa, M. Takizawa, O. Sato, Irradiation Effects on concrete structures, Int. Symp. On the Ageing Manag. Of Nucl. (2012).

[10] H. K. Hilsdorf, J. Kropp, H. J. Koch, The Effects of Nuclear Radiation on the Mechanical Properties of Concrete, ACI SP-55, 1978.

Probability density function of the number of adsorbed beads $N\Lambda$. Effect of Weissenberg number is illustrated

Probability density function of the number of adsorbed beads $N\Lambda$. Effect of Weissenberg number is illustrated

Effect of shear rate and surface potential on particle interaction and aggregation in nanofluids

L. F. Mortimer & M. Fairweather
School of Chemical and Process Engineering, University of Leeds, Leeds, LS2 9JT
l.f.mortimer@leeds.ac.uk, m.fairweather@leeds.ac.uk

1. Introduction

- Decontamination of legacy nuclear waste storage ponds and silos is of great importance and stands as a matter of increasing urgency throughout the nuclear industry.
- In facilities around the UK, waste suspension flows transport legacy material from historic ponds to other interim locations where they are safely stored.
- The modification of multiphase flows to instigate settling behaviour is a promising technique, although the dynamics associated with variation of the surface potential and subsequent stability conditions are presently not well understood on the micro- and nano-scales.
- Since the macro-scale properties and behaviour of nanofluids depend on the underlying micro- and nano-scale interactions, development of understanding of the interaction physics is paramount to full predictive and behaviour control capabilities.
- The challenges associated with generation of understanding surrounding nanoparticulate interaction dynamics in various particle-laden systems will be addressed through use of high-fidelity multiscale simulation techniques.

2. DLVO theory

- Calculations of intersurface forces responsible for aggregation are conventionally described by the well-known DLVO theory (Derjaguin and Landau 1941, Verwey and Overbeek 1948), which accounts for the van der Waals and electrostatic double layer forces.

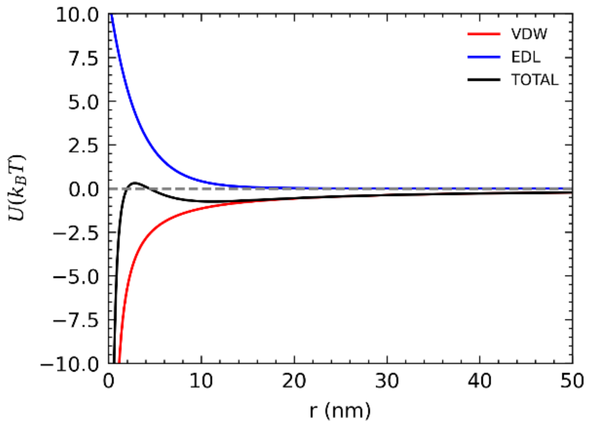

Van der Waals: A short-range attractive interaction, a consequence of quantum dynamics.

Electric double layer: Accounts for the electrostatic repulsion of the double layer, which aids to stabilize the suspension.

3. Langevin dynamics simulations

- Langevin dynamics simulations are performed in both stagnant and shear flows.
- The geometry considered in this study is a $1.35\mu m \times 1.35\mu m \times 2r_P$ cuboid cell, with particles fixed in the $z = 0$ plane, with $r_p = 25nm$.

ANIMATION

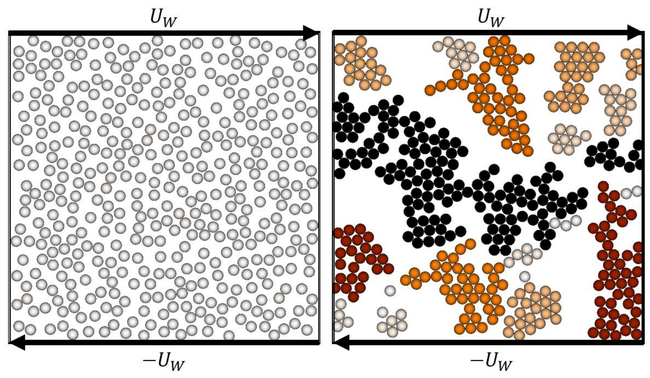

DEMONSTRATION OF LANGEVIN DYNAMICS PREDICTION OF NANOFLUID UNDER SHEAR. COLOUR INDICATES CLUSTER SIZE.

- The nanoparticle motion is solved for using the Newtonian force balance equation below with constant timestep of $\Delta t = 0.01ns$. Simulations were performed for $t_F = 10\mu s$.

$$m_P \frac{d\boldsymbol{u}_P}{dt} = \boldsymbol{F}_D + \boldsymbol{F}_{VDW} + \boldsymbol{F}_{EDL} + \boldsymbol{F}_{SS} + \boldsymbol{F}_B$$

$$\boldsymbol{F}_D = -\zeta(\boldsymbol{u}_P - \boldsymbol{u}_F) \quad \boldsymbol{F}_{VDW} = \frac{Ar_p}{12\delta r^2} \quad \boldsymbol{F}_{EDL} = \frac{2\pi r_p^2 \sigma_C}{\epsilon_0 \epsilon_r \kappa} \mathrm{e}^{-\kappa\delta r} \quad \boldsymbol{F}_{ss} = \frac{4}{3}\sqrt{r_{eff}} E_{eff} \delta r^{3/2} \quad \boldsymbol{F}_B = \sqrt{\frac{6\zeta T k_B}{\Delta t}}$$

FLUID DRAG | VAN DER WAALS | ELECTRIC DOUBLE LAYER | SOFT SPHERE INTERACTION | BROWNIAN MOTION

4. Simulation setup

Parameter	SIM1	SIM2	SIM3	SIM4	SIM5
$r_P(nm)$	25	25	25	25	25
$A\ (10^{-21}J)$	22.3	22.3	22.3	22.3	22.3
$\psi\ (mV)$	1	5	15	20	30
$I\ (M)$	0.01	0.01	0.01	0.01	0.01
$E\ (10^6 Pa)$	72.35	72.35	72.35	72.35	72.35
$\nu_P\ (-)$	0.31	0.31	0.31	0.31	0.31

- Simulation parameters are chosen to match calcite in water, a commonly used experimental simulant for nuclear waste material.

r_p: Particle radius
A: Hamaker constant
ψ: Surface potential
I: Ionic strength
E: Elastic modulus
ν_p: Poisson's ratio

5. Stagnant behaviour

- These figures demonstrate the effect of increasing the surface potential on the stagnant nanoparticulate suspension.
- It is observed that increasing the potential beyond ψ=5mV reduces the mean radius of gyration of particle clusters.
- The coordination number, defined as the mean number of connected neighbour particles, also decreases as the surface potential is increased, with the majority of particles possessing no immediate neighbours for the ψ=30mV system, indicating stabilization.

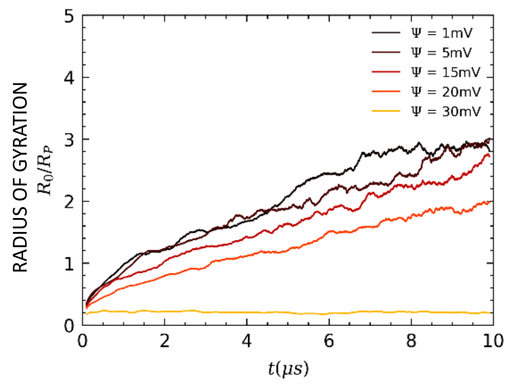

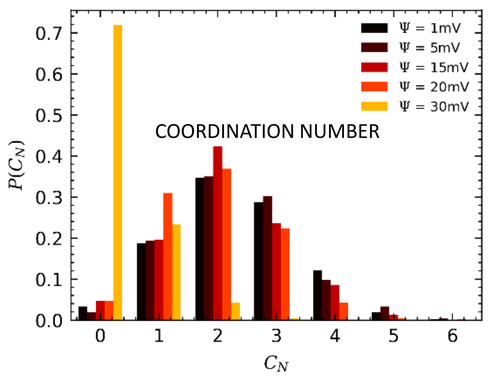

- Below we demonstrate the effect of increasing the surface potential, ψ, on aggregation dynamics in a stagnant flow field by studying instantaneous conformities of particles suspended in a stagnant flow.

$\psi = 5mV$ $\psi = 20mV$ $\psi = 50mV$

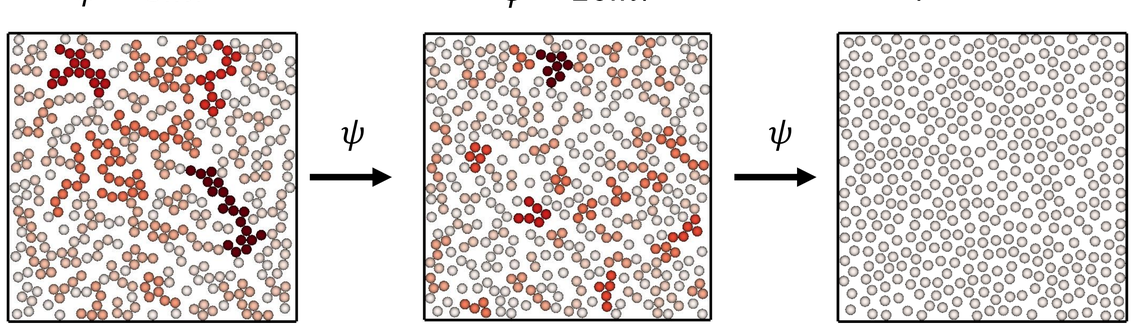

6. Shear behaviour

- The below figures demonstrate the effects of shear rate on nanoparticle clustering dynamics within the system.
- Similar aggregation rates are observed for low shear rates $10^3 \leq \dot{\gamma} \leq 10^5$), whereas by $\dot{\gamma} = 10^6\ s^{-1}$ the aggregation rate almost doubles.
- The hydrodynamic trajectories of the particles induced by the shear lead to more frequent interactions, providing enough energy to overcome the electric double-layer repulsion.
- Beyond, increased shear rates hinder the process, greatly reducing the rate and leading to much lower mean coordination numbers.

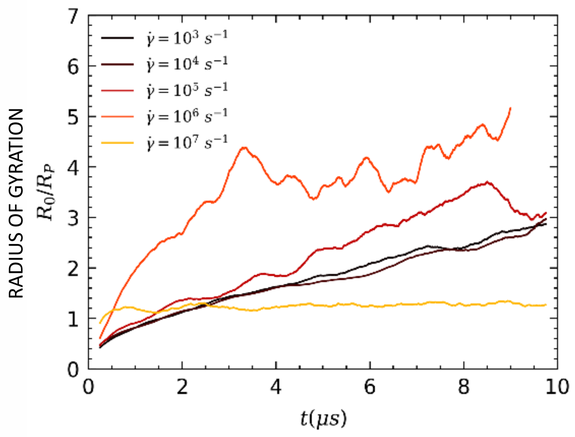

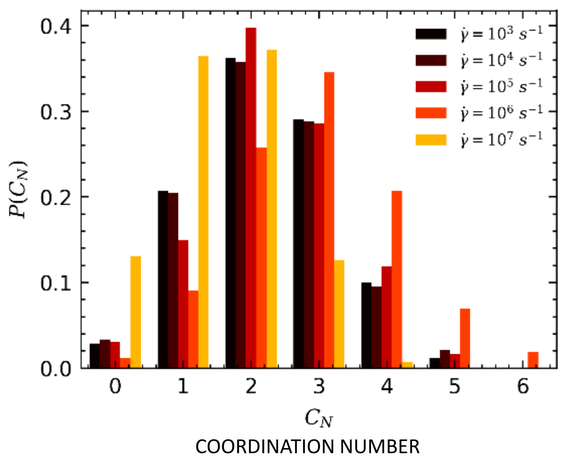

COORDINATION NUMBER

6. Conclusions

- Calcite-water nanoparticulate suspensions have been simulated using Langevin dynamics and DLVO interaction in order to study the effect of surface potential and shear rate on aggregation dynamics.
- It has been demonstrated that reducing the surface potential instigates increased aggregation in stagnant flows. Under shear conditions, particles undergo aggregation up to $\dot{\gamma} = 10^6\ s^{-1}$, beyond which the clustering processes are hindered.

Transformative Science and Engineering for Nuclear Decommissioning

UKRI Engineering and Physical Sciences Research Council

transcendconsortium.org

Energy For a Low Carbon Future

Helium Diffusion in Plutonium Dioxide

Elanor Murray[a*], Ying Zhou[b], Peter Slater[a], Roger Smith[b], Pooja Goddard[b], Helen Steele[c]
[a]School of Chemistry, University of Birmingham, [b]School of Science, Loughborough University, [c]Sellafield LTD, Cumbria
*exm350@student.bham.ac.uk

Introduction

Radiogenic helium gas generation naturally occurs in the ageing of PuO_2 due to the spontaneous alpha decay of Pu isotopes, creating self-radiation damage to the lattice [1]. The accumulation of helium atoms into bubbles could lead to pressurisation of storage cannisters. As such, it is crucial to develop understanding of helium diffusion in PuO_2. This study uses molecular dynamics to investigate the diffusion of helium in PuO_2 for the first time. The system sizes were 8x8x8 supercells, with simulation times of 5 ns over a 1000 – 3000 K temperature range.

Diffusion Regimes

A PuO_2 system with 0.5% He in interstitial sites was evolved using molecular dynamics at 100 K intervals; the diffusivity was calculated via the Einstein relation. Fig.1 plots the diffusivity of He, O and Pu calculated at each temperature. Three regions of interest (R1, R2 and R3) are highlighted:

- R1 (1000-1500 K): There is no diffusion. Here atoms only vibrate around their lattice sites over the simulation time scale.
- R2 (1500-2500 K): The diffusivity of He and O increases with increasing temperature, with their diffusion closely aligned. This suggests the main helium diffusion mechanism is oxygen vacancy assisted. Fig 2. displays an example of oxygen vacancy assisted diffusion at 2100 K.
- R3 (>2500 K): The oxygen diffusion levels off, which may be due to the oxygen sub lattice going through a Bredig phase transition and becoming amorphous [3]. Also in this region plutonium diffusivity increases. It is possible that the helium diffusivity plateau could be due to plutonium vacancies becoming available and trapping helium.

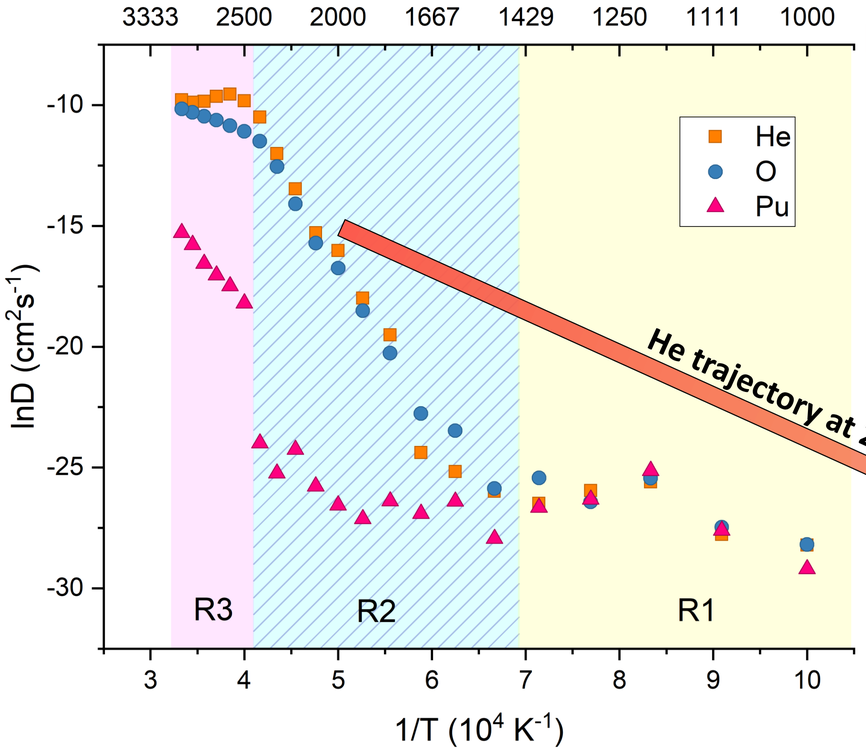

Fig 1: Diffusivity as a function of temperature for helium, oxygen and plutonium in PuO_2 with 0.5% He concentration.

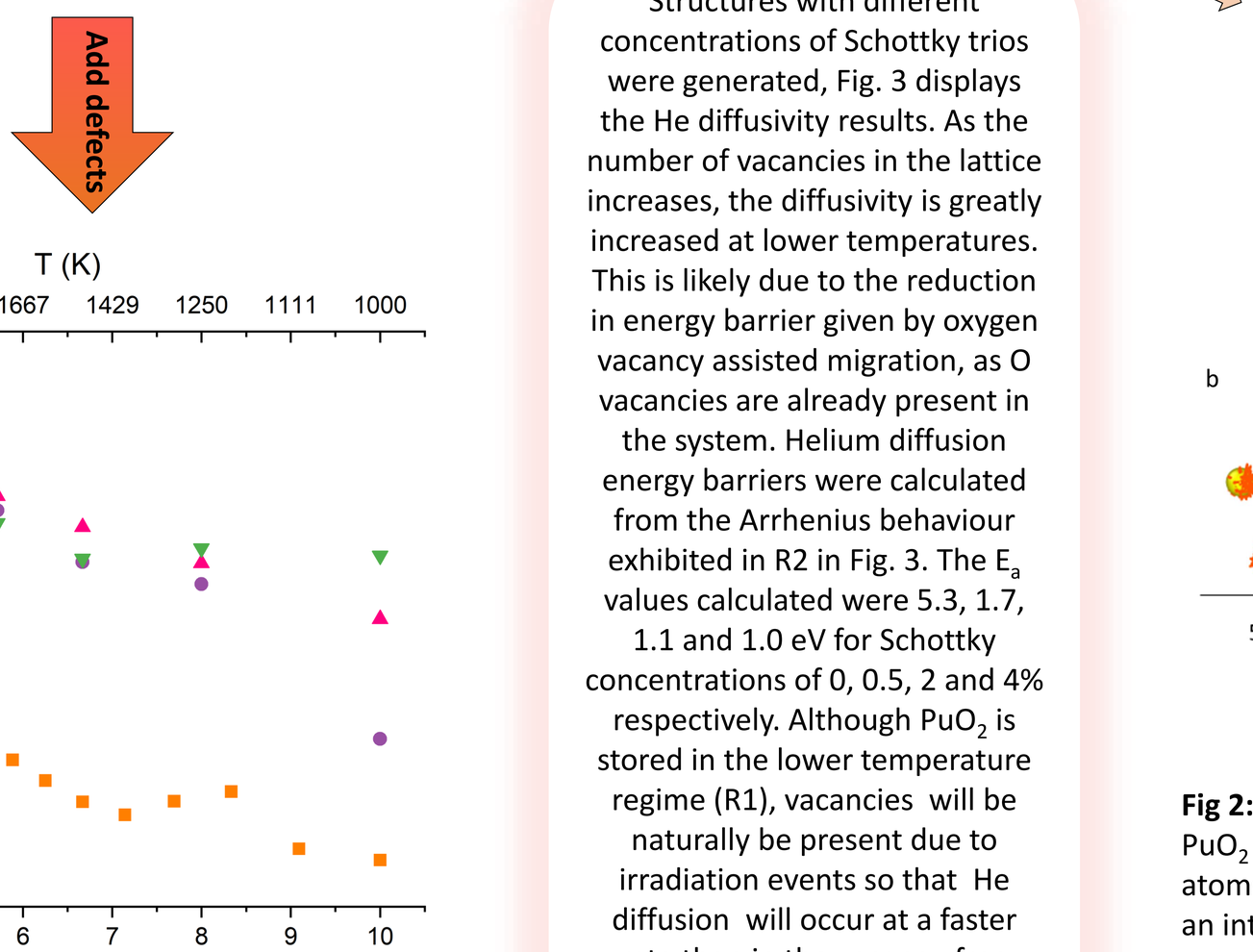

Defects

Structures with different concentrations of Schottky trios were generated, Fig. 3 displays the He diffusivity results. As the number of vacancies in the lattice increases, the diffusivity is greatly increased at lower temperatures. This is likely due to the reduction in energy barrier given by oxygen vacancy assisted migration, as O vacancies are already present in the system. Helium diffusion energy barriers were calculated from the Arrhenius behaviour exhibited in R2 in Fig. 3. The E_a values calculated were 5.3, 1.7, 1.1 and 1.0 eV for Schottky concentrations of 0, 0.5, 2 and 4% respectively. Although PuO_2 is stored in the lower temperature regime (R1), vacancies will be naturally be present due to irradiation events so that He diffusion will occur at a faster rate than in the vacancy-free system.

Fig 3: Helium diffusivity as a function of temperature for four different Schottky defect concentrations in PuO_2 with 2% helium concentration.

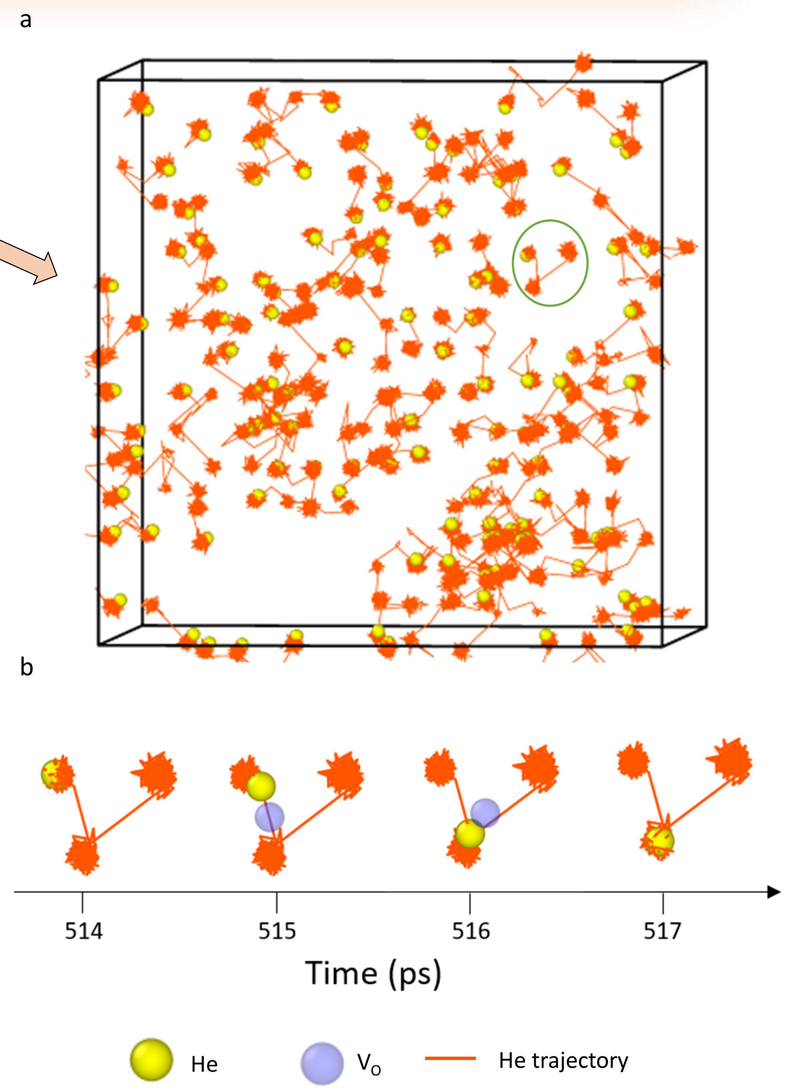

Fig 2: Trajectories of He atoms in initially defect-free PuO_2 at 2100 K. a) displays the trajectory of all He atoms over a period of 1ns. b) displays a snapshot of an inter-site hop by a He atom from the area circled in green in a). The time period in b) is 514-517 ps. It can be seen that at 515 ps an oxygen vacancy is generated in the vicinity of the helium and the helium uses this to migrate to a neighbouring OIS.

Conclusions

In defect free PuO_2, He exhibits limited diffusive behaviour until the temperature exceeds 1500 K. However, we have found that when vacancies are present within the lattice, the He diffusion energy barrier is significantly reduced and He atoms exhibit diffusive behaviour at lower temperatures. Therefore whilst the storage of PuO_2 will be at temperatures well below 1500 K, due to the presence of defects within the lattice we suggest that He will be mobile during storage. The main He diffusion mechanism proposed is oxygen vacancy assisted inter-site hops with helium and oxygen having comparable diffusion rates.

References: [1] W. G. Wolfer, Los Alamos Sci., 2000, 26, 274–285, [2] H Mehrer, Diffusion in Solids, Springer, 2007, [3] M. W. D. Cooper, S. T. Murphy, M. J. D. Rushton and R. W. Grimes, J. Nucl. Mater., 2015, 461, 206–214. *The computations described in this poster were performed using the University of Birmingham's BlueBEAR HPC service.*

Radiation effects on nuclear waste forms: How does the crystallinity of glass composite affect radiation tolerance?

Tamás Zagyva[1], Robert Harrison[1], Tracey Taylor[2], Mike Harrison[2], Laura Leay[1], Brian O'Driscoll[3]

[1]The University of Manchester [2]National Nuclear Laboratory [3]The University of Ottawa

Correspondence: tamas.zagyva@postgrad.manchester.ac.uk

1. Introduction

The washout of the Highly Active Storage Tanks at Sellafield during the post-operational clean out (POCO) will generate a radioactive waste stream rich in Mo-containing solids [1]. This waste will be converted into a solid and durable form for long-term disposal. The final waste form is a Ca/Zn borosilicate glass composite material containing powellite ($CaMoO_4$) crystals.

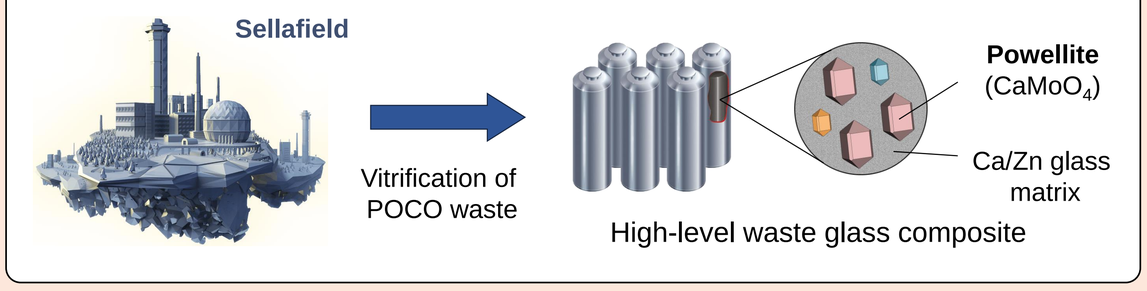

Goal of research: Characterise Mo-rich nuclear waste simulant glass composites and evaluate their long-term radiation tolerance by performing heavy ion irradiation experiments.

2. Materials & Methods

- Mo-rich non-active waste simulant glass composites were produced by National Nuclear Laboratory in the Vitrification Test Rig (VTR).
- Nickel and gold ion irradiation experiments were performed to induce changes similar to alpha recoil nuclei. The average total dose was ~ 1.4 displacements per atom (dpa) in powellite, equivalent to 1.0-1.3 GGy dose.

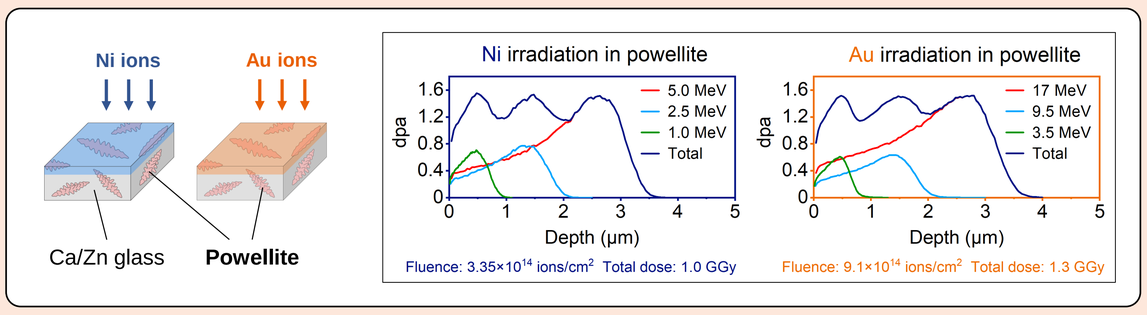

- X-ray diffraction (XRD), scanning electron microscopy (SEM), electron backscatter diffraction (EBSD), and transmission electron microscopy (TEM) (with *in situ* Ar & Xe irradiation) were used for characterisation.

3. Radiation tolerance of glass composites

The main crystal phases in the waste simulant samples were powellite, zircon, cerianite, zincochromite and ruthenium dioxide. Microcracks formed around large powellite and zircon crystals, presumably due to a thermal expansion mismatch between the glass and these phases.

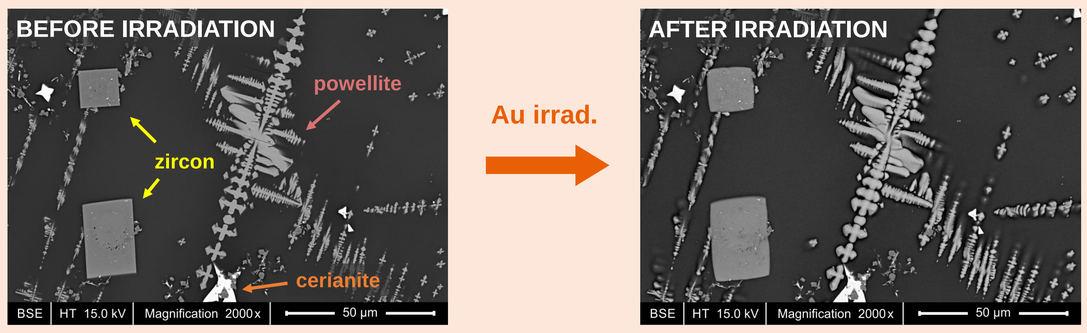

Powellite and zircon swelled considerably after Ni and Au irradiation. The radiation damage was greater in the Au irradiated sample.

EBSD analysis shows the relative radiation tolerance of phases.

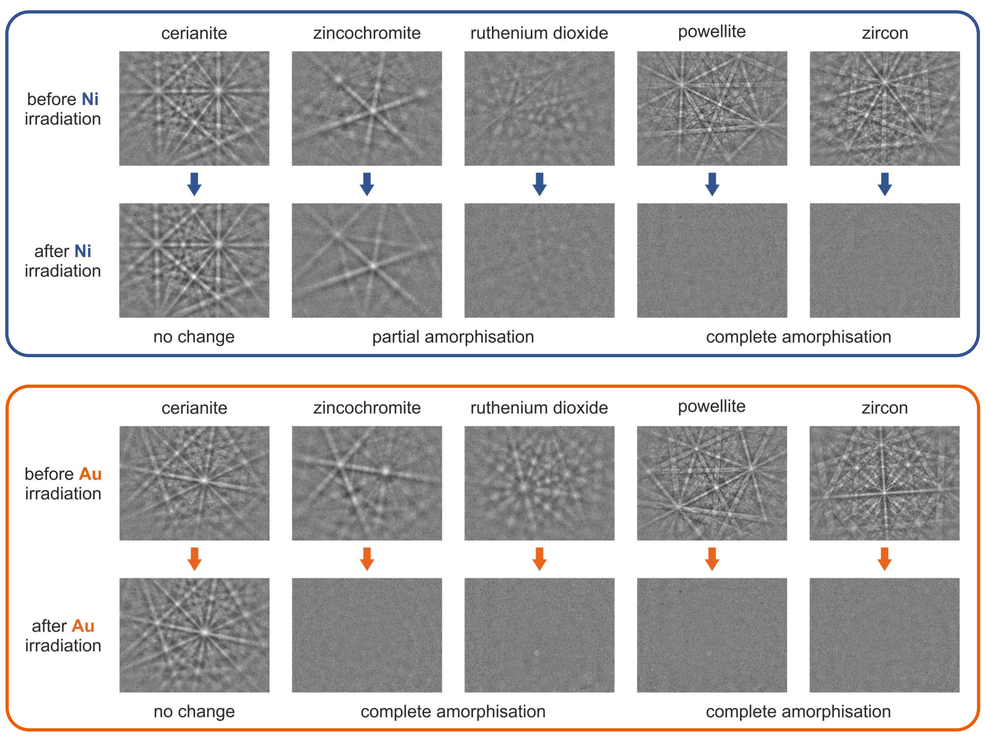

4. TEM with *in situ* Ar and Xe ion irradiation on powellite

- Ar, Xe and Pb irradiations published in the literature suggest that powellite is highly radiation-tolerant as it remains crystalline at high fluences [2-4].
- However, our *in situ* Ar and Xe ion irradiation experiments show that amorphisation could occur depending on the temperature and ion type.

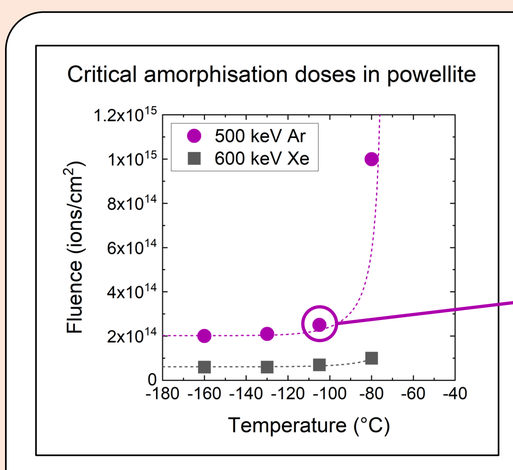

TEM analysis above -80 °C was not possible because of the electron beam-induced recrystallisation.

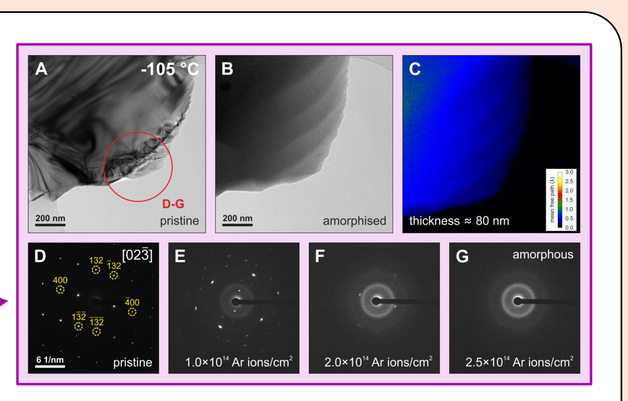

Bright-field (A,B), diffraction (D-G) images and thickness map (1 λ = 159 nm) of Ar-irradiated powellite. Diffraction pattern with bright spots represents crystalline structure, diffuse rings correspond to amorphous material.

5. Conclusions

- Ni and Au ion irradiation experiments reveal insights into the relative radiation tolerance of crystals (cerianite > zincochromite ≈ ruthenium dioxide > powellite ≈ zircon).
- We presented the first evidence of powellite amorphisation under heavy-ion irradiation. Powellite is less radiation tolerant than previously thought [2-4].
- The amorphisation of powellite in the previous studies was not observed either due to the recombination of intracascade close-pairs [2,4] or due to the ionisation-induced damage recovery [3-4].
- The radiation-induced swelling of powellite and zircon is likely to cause considerable stress in the glass composite that might lead to the formation of continuous extensive cracks on geologically relevant time-scales.

6. Acknowledgements

Special thanks to Anamul Haq Mir for the TEM measurements at the MIAMI irradiation facility, Chetna Tyagi for the XRD measurements, and Györgyi Glodán for the SEM training. I am also grateful to Samir de Moraes Shubeita and the DCF ion beam accelerator team for the nickel and gold irradiation experiments.

7. References

[1] Harrison, 2017, Vitrogeowastes, Chapter 3, pp. 33-76.
[2] Wang et al. 2014, Journal of Raman Spectroscopy, vol. 45, pp. 383-391.
[3] Patel et al. 2018, Journal of Nuclear Materials, vol. 510, pp. 229-242.
[4] Mendoza et al. 2011, Optical Materials, vol. 34, pp. 386-390.

Assessing the strength of biomineral strategies for concrete repairs

PhD Student: Thanos Karampourniotis

5th floor, James Weir Building, University of Strathclyde, Glasgow

E-mail address: athanasios.karampourniotis@strath.ac.uk

Professor Rebecca Lunn[1], Dr. Enrico Tubaldi[2], Dr. Grainne El Mountassir[3], Dr. Gloria Castro Quintero[4]

[1,2,3,4]Department of Civil and Environmental Engineering, Faculty of Engineering, University of Strathclyde, Glasgow, United Kingdom

Problem Introduction

Nuclear Decommissioning

- Most of the UK's nuclear power stations were built from late 1970 to late 1980, with most of them closing by 2030.
- The harsh environment and conditions these assets are exposed to, leads to degradation and cracking of concrete.
- We must guarantee the safety of the structures, until the decommissioning process is completed.

More attention should be given to effectively repair and maintain the existing structures and infrastructure.

New repair technique – MICP

Microbially Induced Carbonate Precipitation (MICP) is a novel concrete repair method that takes advantage of bacteria like S. Pasteurii where together with urea and a calcium source can form calcium carbonate ($CaCO_3$) crystals.

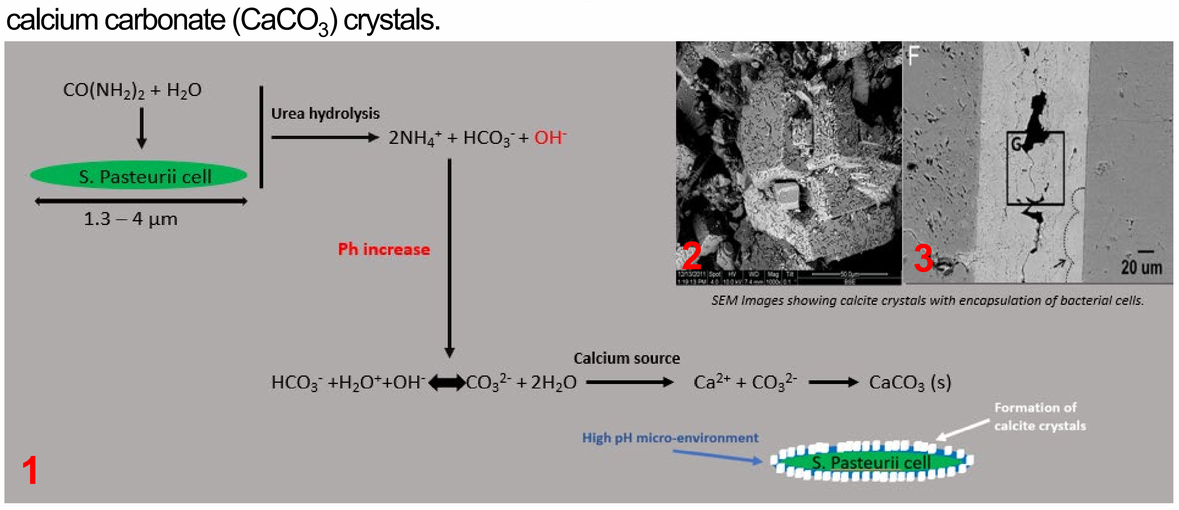

SEM Images showing calcite crystals with encapsulation of bacterial cells.

Figure 1: Schematic of the MICP method.

Figure 2: SEM image presenting calcite crystals with encapsulated bacteria. [1]

Figure 3: SEM image showing the growth of calcite crystals in layers. [2]

Experiments

Methodology

Five degraded concrete cores with an initial fracture aperture of 0.5mm with the use of glass beads on the corners, were treated with MICP. Core 1 had no fill material (**Figure 4**), Core 2 had six patches of glass beads in the middle (**Figure 5**) , whereas Core 3 (**Figure 6**) was packed with sand (150μm-212μm in diameter). Cores 4 and 5 were packed with glass beads (**Figure 7**).

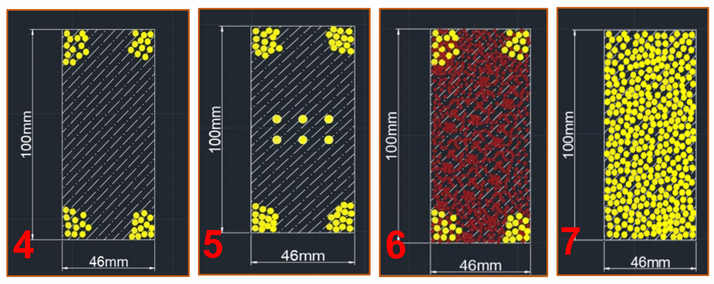

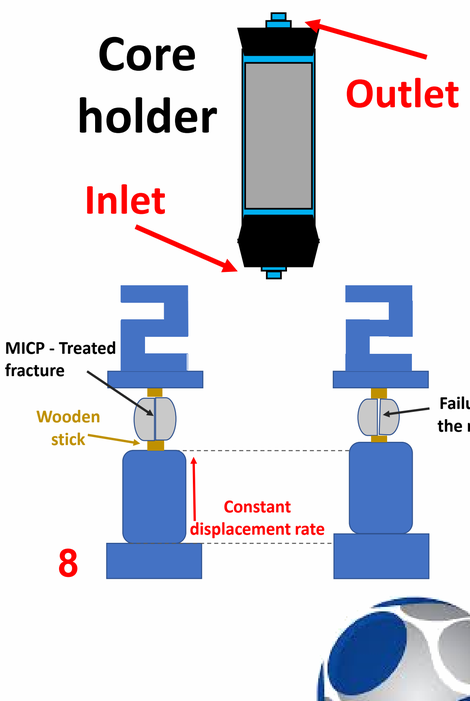

Each MICP treatment involves the injection of a bacterial solution, followed by a cementing solution (calcium chloride and urea). Afterwards, hydraulic conductivity measurements monitor calcite precipitation (**Figure 9**).

Subsequently, when the core is repaired, characterization of the sealed fracture includes X-Ray Computed Tomography (XCT) scanning and tensile strength quantification via the Brazilian test/splitting test (**Figure 8**).

MICP Cycles Monitoring

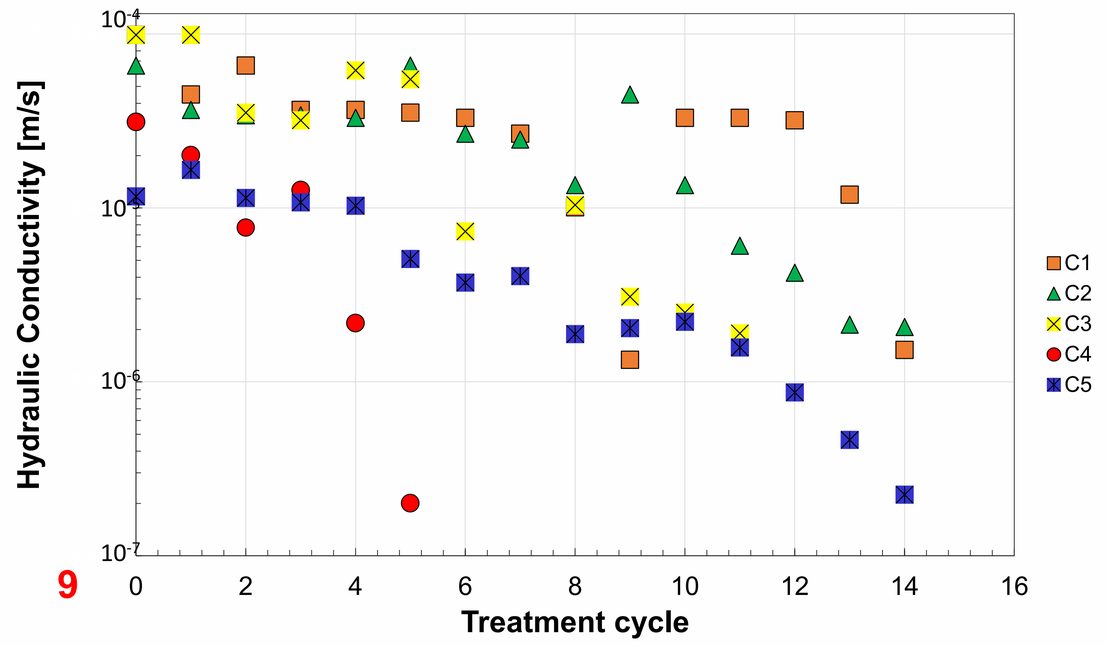

Results

After the MICP treatments, Cores 1, 2 and 3 were subjected to XCT-scanning and image analysis (**Figures 10, 12** and **14** respectively) to investigate the distribution of contact points in the fractures. White pixels represent the contact points that bridge the initial gap and black pixels represent the regions where there is no contact. Comparing the processed XCT images with the observed distribution of calcite after the specimens' failure (**Figures 11, 13** and **15**), common features can be noticed confirming the validity of the image analysis conducted.

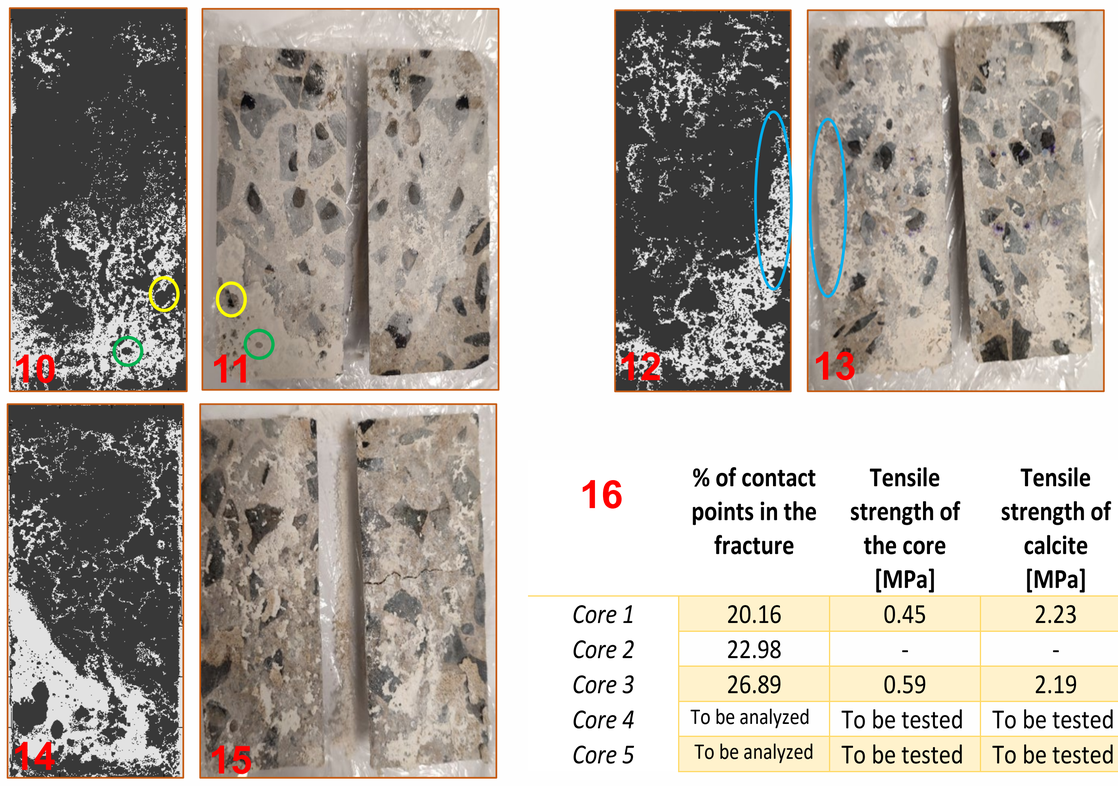

16	% of contact points in the fracture	Tensile strength of the core [MPa]	Tensile strength of calcite [MPa]
Core 1	20.16	0.45	2.23
Core 2	22.98	-	-
Core 3	26.89	0.59	2.19
Core 4	To be analyzed	To be tested	To be tested
Core 5	To be analyzed	To be tested	To be tested

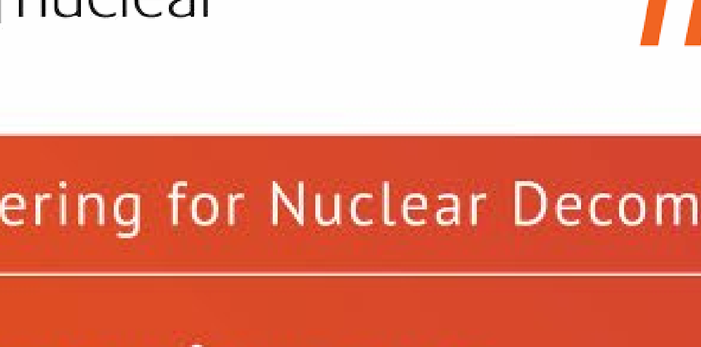

Five degraded concrete cores have been repaired using the MICP technique (**Figure 16**). Cores 1, 2 and 3 have been analyzed using image analysis software to observe the distribution of calcite crystals. The next step is to analyze the reconstructed images of Cores 4 and 5 and subject them to tensile testing.

The force-time graph of the tensile tests for Cores 1, 2 and 3 display that due to irregularities/cracks on the outer surface, Core 2 was not able to develop enough mechanical resistance during the Brazilian tensile test. (**Figure 17**) .

References

[1]: El Mountassir et al., 2018. Applications of Microbial Processes in Geotechnical Engineering, Advances in Applied Microbiology;104:39-91

[2]:Tobler et al., 2018. Microscale Analysis of Fractured Rock Sealed With Microbially Induced CaCO3 Precipitation: Influence on Hydraulic and Mechanical Performance, Water Resources Research;54:8295-8308

Acknowledgements

This PhD project is funded by Cavendish Nuclear

Transformative Science and Engineering for Nuclear Decommissioning

transcendconsortium.org

Combining electro-kinetic remediation with colloidal silica grouting in radioactively contaminated soils

Arianna Gea Pagano[1], Frances Burrell[2], Andy Cundy[2], Grainne El Mountassir[1], Rebecca Lunn[1]

[1]Department of Civil and Environmental Engineering, University of Strathclyde, Glasgow
[2]School of Ocean and Earth Science, University of Southampton

Electrokinetic Remediation (EKR) of radioactively contaminated soils

Electro-kinetic remediation: remediation technique using a low-voltage, direct-current electric field applied across a section of contaminated soil to move contaminants.

A: Electro-migration
B: Electrophoresis
C: Electro-osmosis

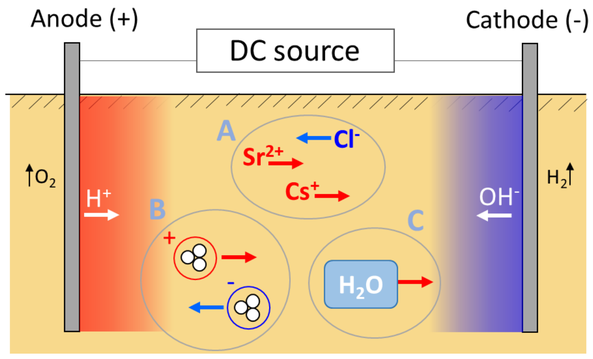

The pH gradient helps mobilise surface-bound contaminants into pore water in soluble ionic form. The movement of water (electroosmosis) and other ions (electromigration) in this electric field helps concentrate contaminants in specific regions, usually around electrodes, thus minimising the total volume of contaminated soil. This technique works well with a wide range of inorganic contaminants and metals.

COLLOIDAL SILICA GROUT TREATMENT:

Colloidal silica is an aqueous suspension of silica nano-particles (SiO_2). The creation of siloxane bonds (Si – O – Si), triggered by the addition of an electrolyte accelerator, leads to the formation of a network of silica nanoparticles in the form of a hydrogel.

'Purge & trap' concept

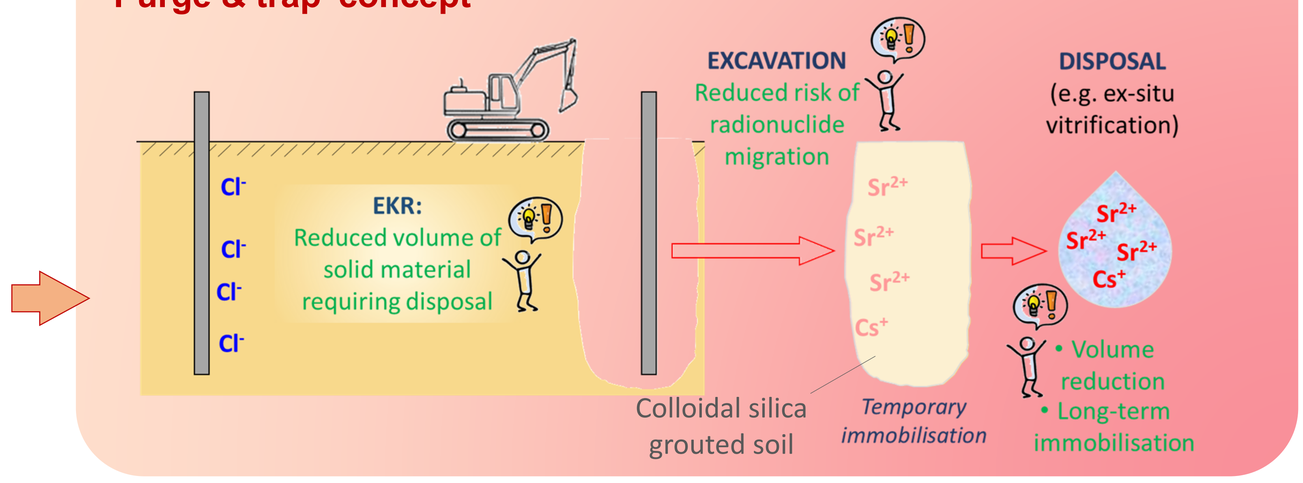

Experimental trials

1. EKR run for 4 days (96 hours) at 1 V/cm

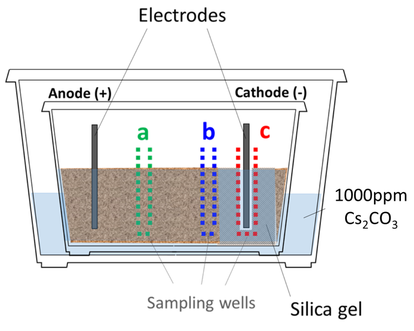

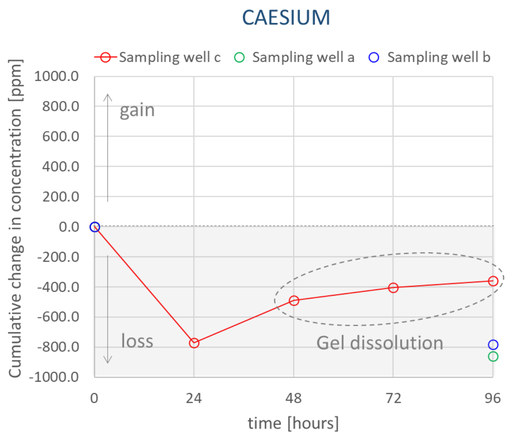

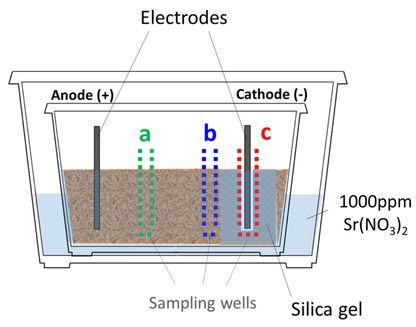

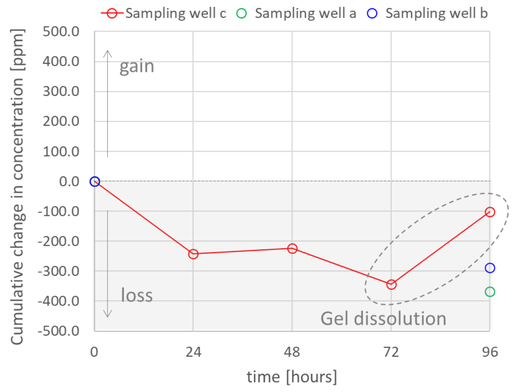

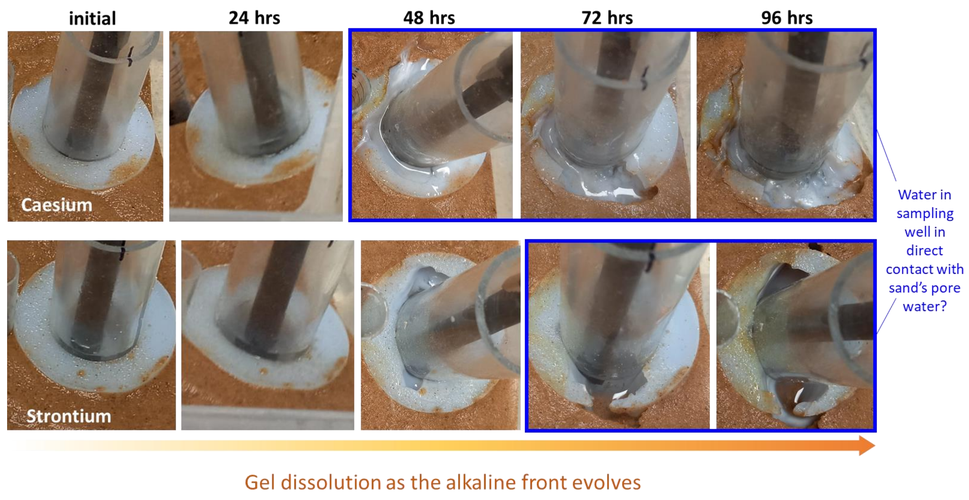

Initial condition:

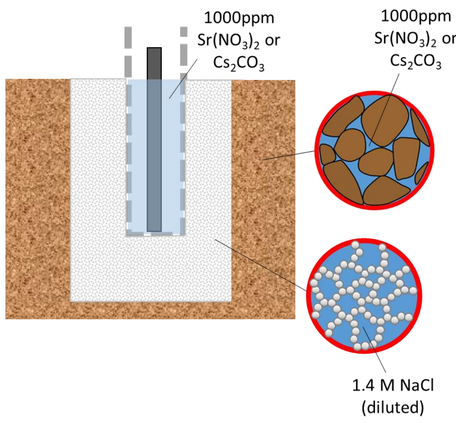

Potential mechanisms of ionic transport:

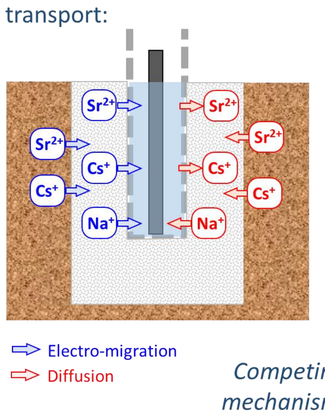

Competing mechanisms!

- ❑ The alkaline front generated at the cathode (pH measured after 24 hours: 12.5) induced the dissolution of the silica hydrogel after 48-72 hours. After silica dissolution, the solution within the well is in direct contact with the sand's pore water, thus undermining the validity of the results.
- ❑ The concentrations of Cs and Sr prior to silica gel dissolution indicate a loss of Cs and Sr from the sampling, which is in contrast with the expected trend for electro-migration.
- ❑ The loss of Cs and Sr is potentially associated to a diffusive mechanism from the sampling well into the silica hydrogel, due to the absence of Cs and Sr ion within the silica hydrogel.

2. EKR run for 6 days (144 hours) at 0.5 V/cm

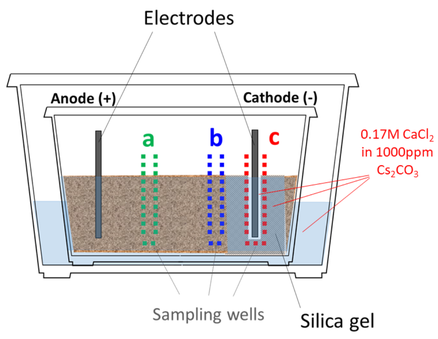

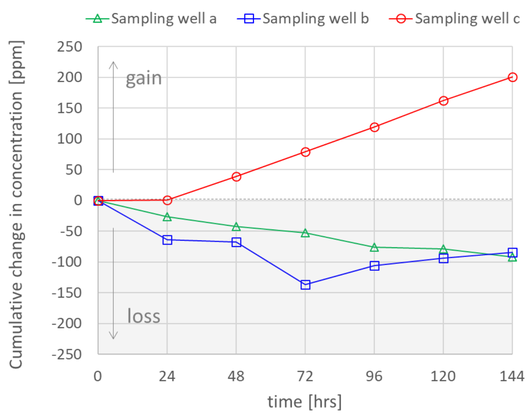

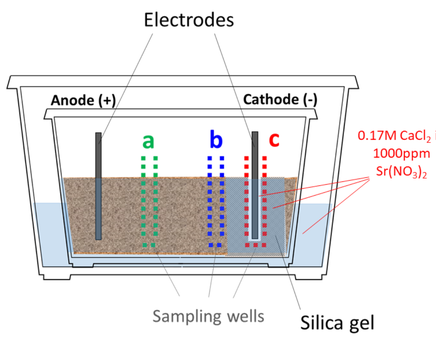

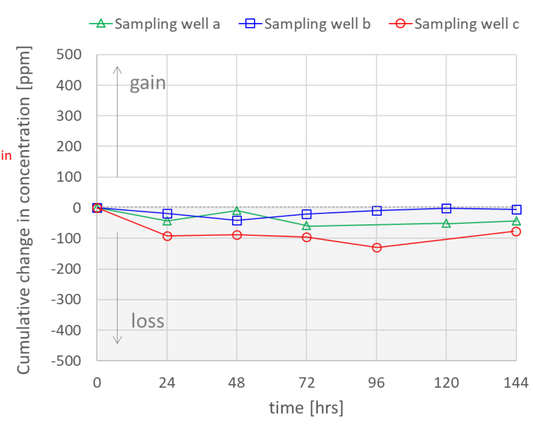

- ❑ Halving the voltage (from 1 to 0.5 V/cm) allowed to prevent silica hydrogel dissolution over the full duration of the experiment.
- ❑ The mobilisation of Cs is in line with the expected trend for electro-migration, with a gain of Cs at the cathode (well c) and a loss of Cs at wells a and b over time.
- ❑ On the other hand, Sr is barely mobilised, with a slight loss overtime at the cathode. This is believed to be associated with the precipitation of Sr salts at the cathode, induced by the alkaline pH.

3. EKR run for 6 days (144 hours) at 0.25 V/cm

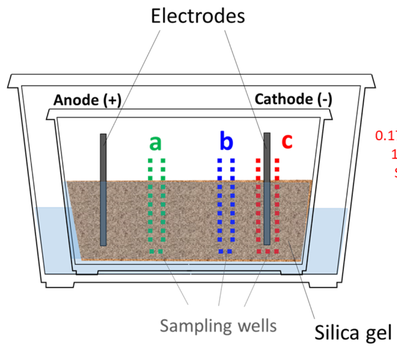

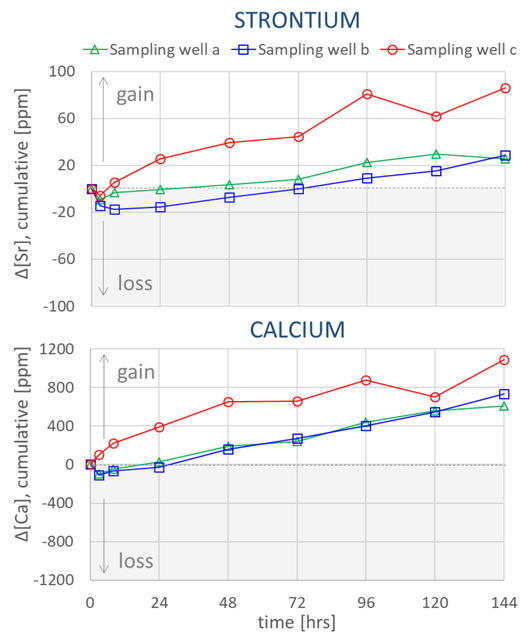

- ❑ Reducing the voltage from 0.5 to 0.25 V/cm allowed to prevent the precipitation of Sr salts at the cathode. The mobilisation of both Sr and Ca follow the expected trend for electro-migration.

Simulation of behavioural modification effects in suspension waste pipe flows.

Bisrat Wolde
School of Chemical and Process Engineering, University of Leeds
pmbw@leeds.ac.uk

Introduction:

The ability to predict particle dispersion, particle-particle interaction, deposition and agglomeration effectively within fluid flows can improve nuclear waste management operations, and in particular the retrieval of such waste and post-operational clean-out (POCO) operations. In the present work, by using high-accuracy and robust simulation techniques, the impact of behavioural modification techniques on particle dispersion and agglomeration is investigated using a fully-coupled DNS-LPT approach.

Motivation and Objective:

The overall aim is to establish a predictive tool to support POCO operations through improvements in the flow, mixing and separation of wastes during retrieval and POCO operations. In particular, the impact of behavioural modification on particle agglomeration, and hence the likely deposition of particles during processing.

Methodology:

To solve the descriptive equations in a direct numerical simulation the computational fluid dynamics solver Nek5000 has been used. This solver is based on the spectral element method that is a high-order weighted residual technique. It is favourable due to its high accuracy, and low numerical dispersion and dissipation, and is easily and efficiently parallelisable. A Lagrangian particle tracker has been developed to model large quantities of dispersed solids which runs concurrently with Nek5000. And then, a fourth order Runge-Kutta method implemented to solve the particle equation of motion for each particle within every time-step.

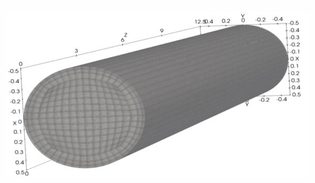

The computational mesh topology:

- A circular pipe of diameter, D,
- Length, L = $12.5D$,
- Partitioned into 36,576 spectral elements.

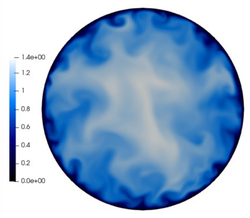

The instantaneous streamwise velocity

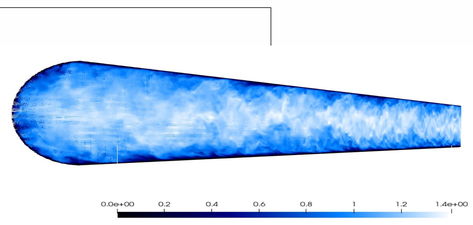

Clipped at the centreline

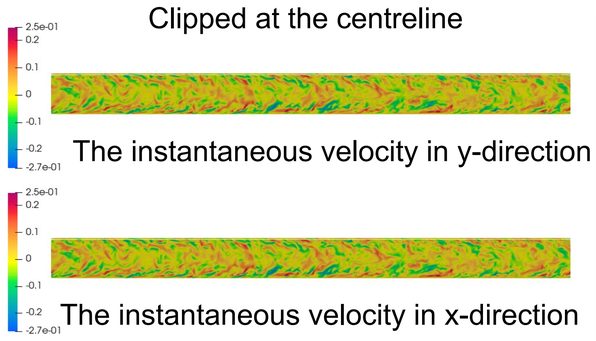

The instantaneous velocity in y-direction

The instantaneous velocity in x-direction

Fluid and Particle Results:

The predictions have been validated and compared with literature simulations and experimental datasets – Fig.1. The outcomes are in good agreement with literature results. Using the fully developed $Re_\tau = 720$ fluid flow computation noted above is being used to simulate one-and four-way coupled flows, and four-way coupled flows with agglomeration, at high concentration with a volume fraction of 10^{-3}. Such a high concentration is required to encourage particle collisions and ensure sufficient agglomeration of particles. Fig.2 to Fig. 4 are the the results obtained using 150,000 randomly injected particles initially assigned the local fluid velocity. 100 μm particles with a density ratio (with the fluid) of 2.71 are being used for all the high concentration simulations. The effect of particle Stokes number on particle deposition within a wall-bounded turbulent flow also investigated – Fig.5.

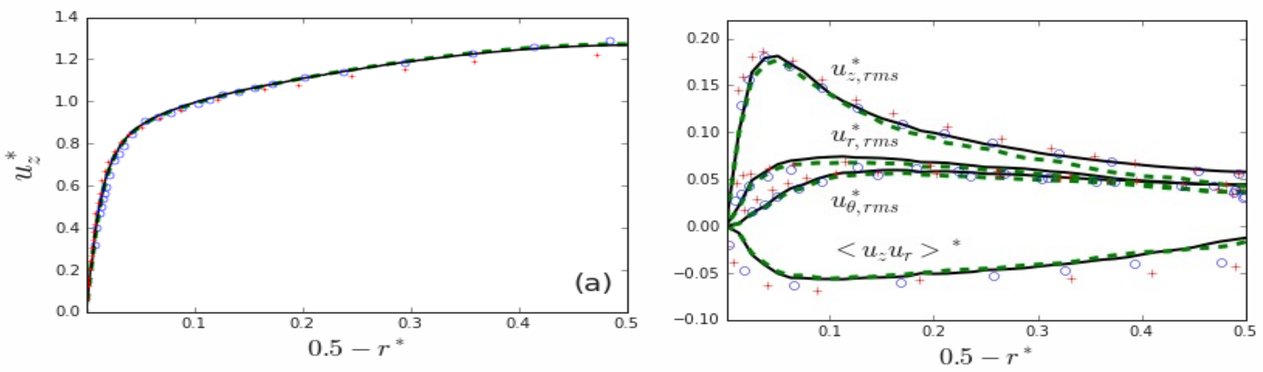

Fig. 1: LPT validation, effects of particle in one-way and four-way coupling. (a) - Mean and (b) - RMS of axial, $u^*_{z,rms}$, radial, $u^*_{r,rms}$, and azimuthal, $u^*_{\theta,rms}$, and Reynolds shear stress, $< u_z \ u_r >^*$. —: present one-way and – –: present four-way coupling. +: and ○ are Rani et al. (2004) one-way and four-way coupled respectively.

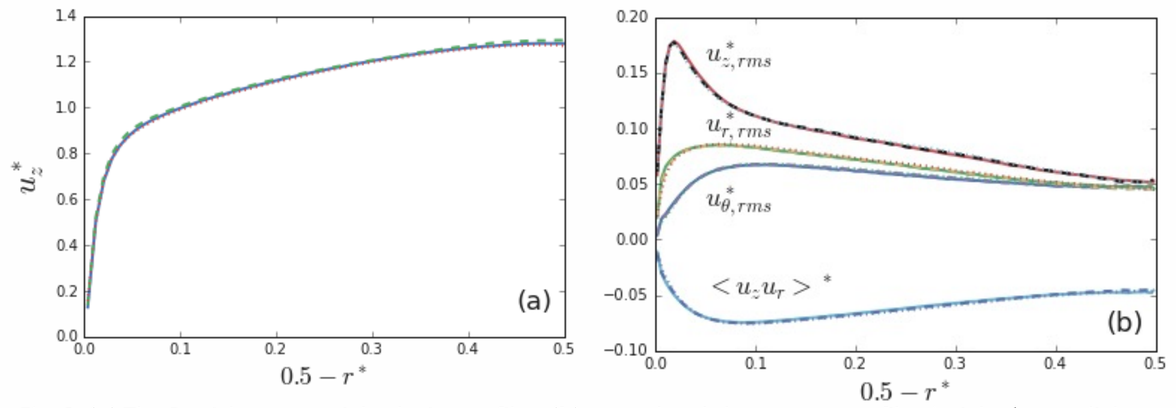

Fig. 2: (a) The Particle mean axial velocity profiles, **(b)** normal and shear stress profiles (axial, z^*_{rms}, radial, r^*_{rms}, azimuthal, θ^*_{rms}, and Reynolds shear stress, $< u_z \ u_r >^*$ as a function of $0.5 - r^*$. —, solid lines are one-way coupling, – –, dashed lines are four-way coupling and ···, dotted lines are four-way coupling with agglomeration.

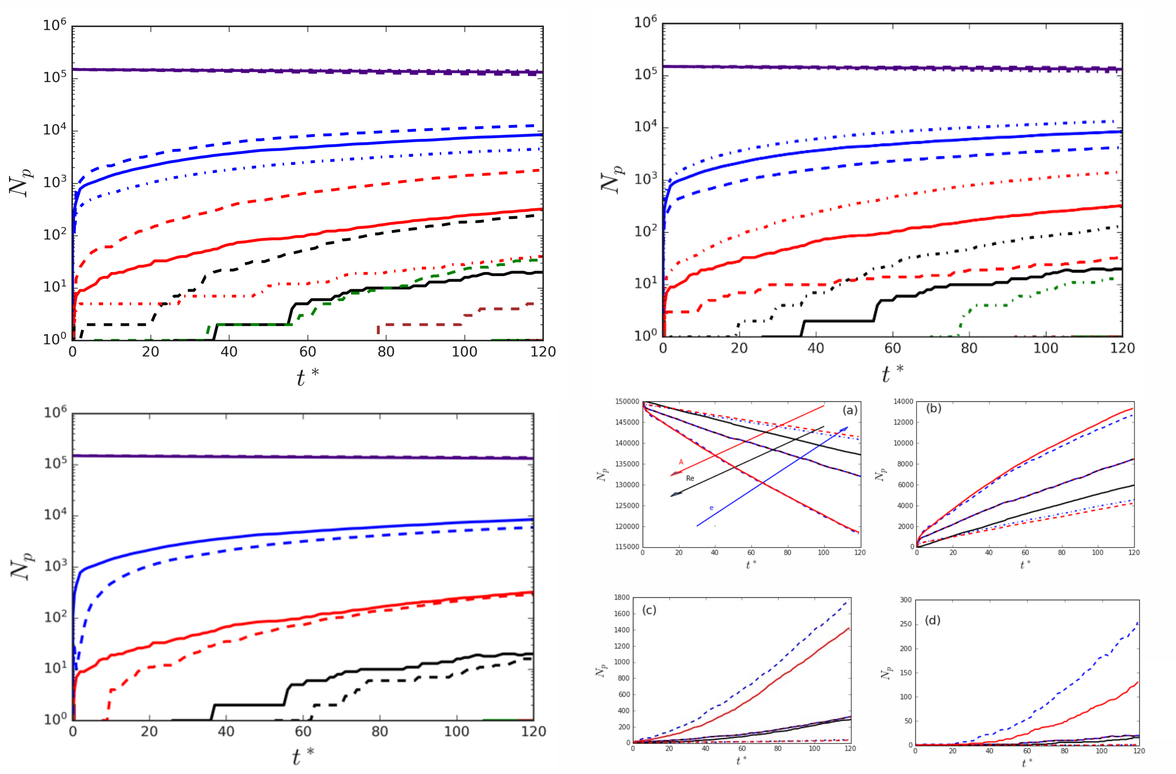

Fig. 3: Influence of the normal restitution coefficient – top left , Hamaker constant – top right, Reynolds number (Re) – lower left and linear plots for all – lower right. The total number of agglomerates of size N as function of t*. Indigo: N= singlets; blue: N = doublets; red: triplets; black: N = quadruplet; green: N = quintuplet and brown: N = sextuplets. ; —: e_n= 0.4, Re =360, A = 36.76zJ , – –: e_n= 0.2, Re = 720,A = 7.84zJ and –·–: e_n= 0.6, A = 22.3zJ.

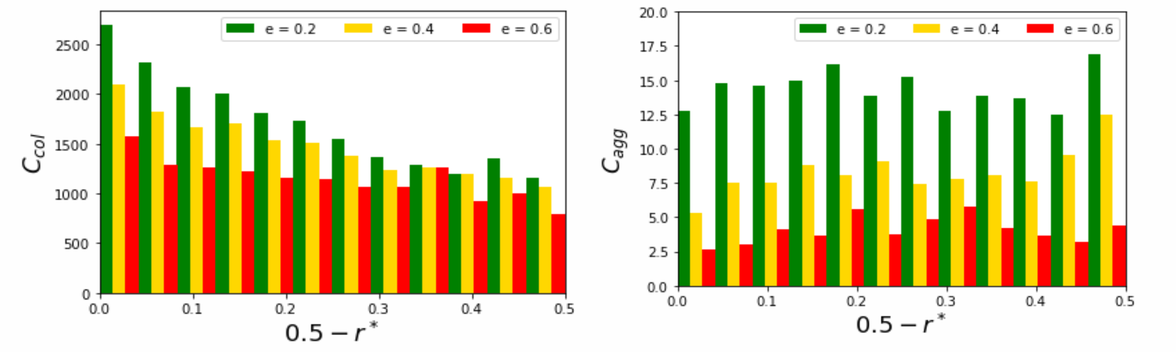

Fig. 4: Effect of variation of coefficient of restitution on the collision and agglomeration concentration at t^* =70, normalised by volume.

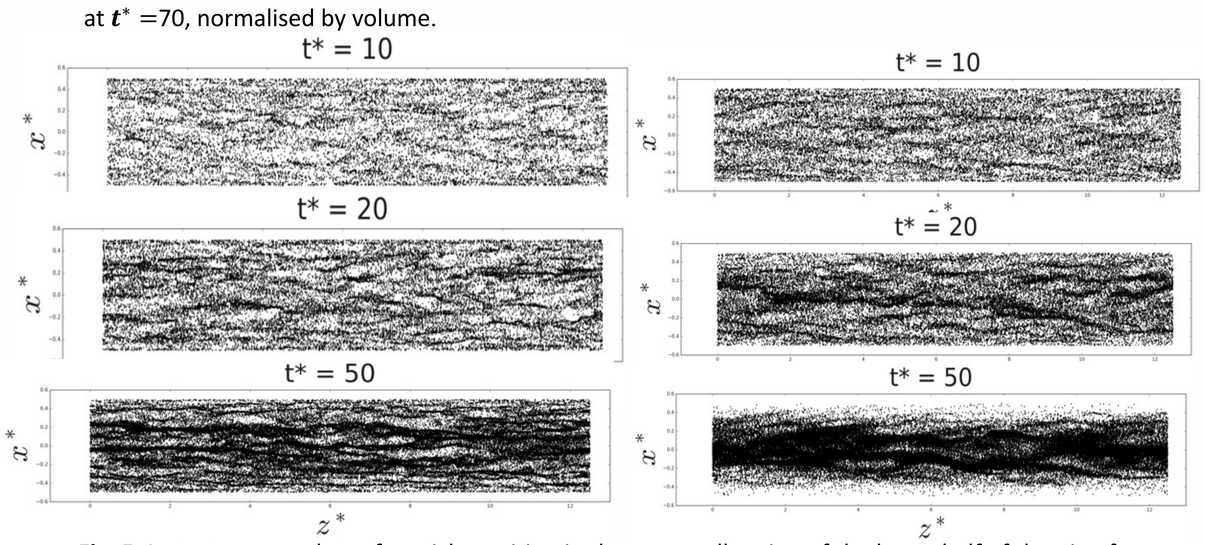

Fig. 5: Instantaneous plots of particle position in the near-wall region of the lower half of the pipe for $St^+ \cong 5.5\ (left)$ and $St^+ \cong 16.78(right.)$

Planned work:

- Finalising the behavioural modification techniques using first principles which has been used to examine effects of flow and solid property changes on particle-laden flow characteristics.

Acknowledgments:

The authors are grateful for funding from the UK Engineering and Physical Sciences Research Council and the University of Leeds through the TRANSCEND (Transformative Science and Engineering for Nuclear Decommissioning) project (EP/S01019X/1).

Understanding caesium's effect on the CAS system due to vitrification

Lucas-Jay Woodbridge
University of Sheffield
lwoodbridge1@sheffield.ac.uk

• Following on from the success seen from vitrification of IONSIV IE-911 an attempt to replicate this result was attempted with the CAS system Therefore suitable pristine glasses were identified that melted at 1450°C.

• Lighter green marks succesful glasses made at 1450, darker green glasses made at 1500 and red failed attempts.

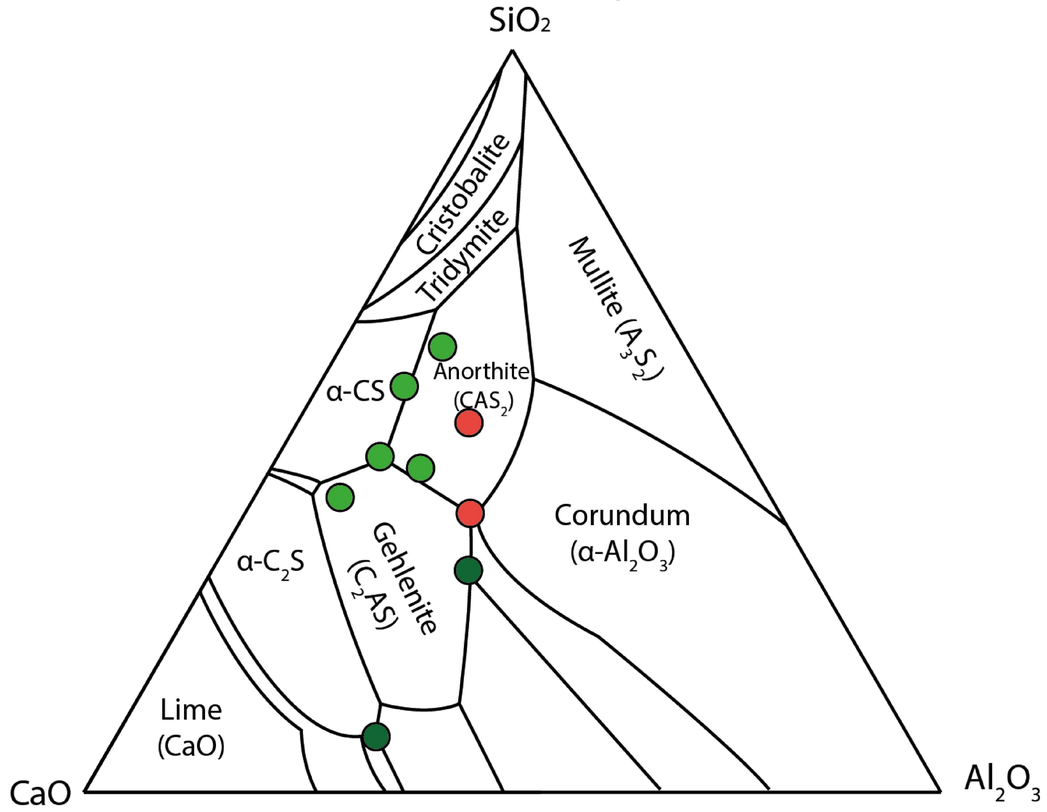

• To investigate what (chemically) was causing this further scopes were undertaken using CAS 50 10 40 as a base and loading 1, 5 and 10% of all the alkali metals into the system to see if it was an element group effect or a size effect/ moving down the group effect.

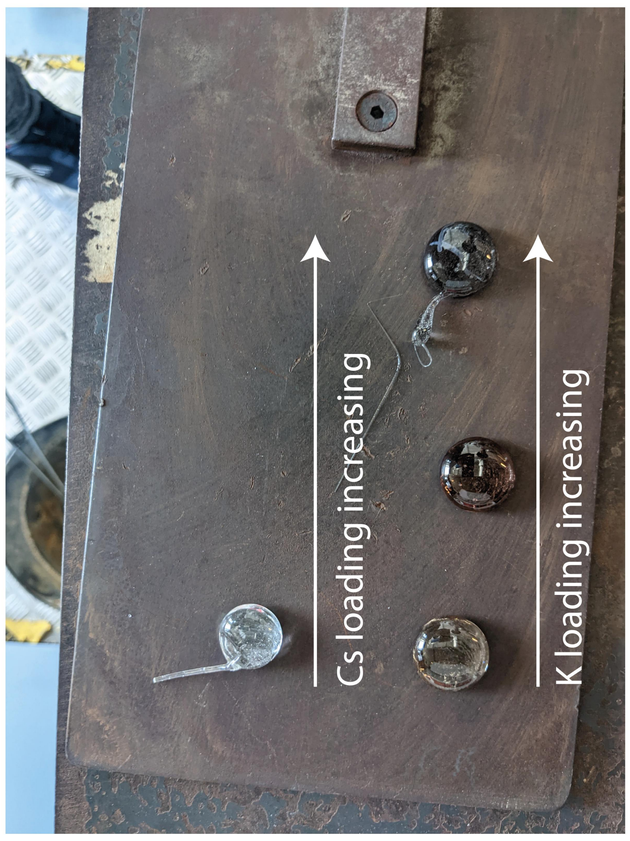

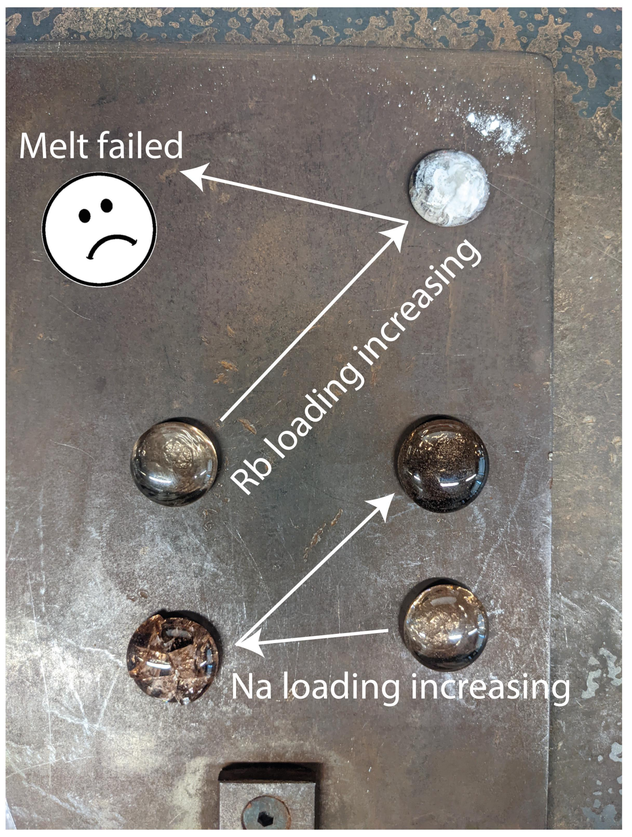

• 5 pristine glasses were achieved. However, once loading of even 1 Mol% Cs the glasses would either pour with significant crystallisation or wouldn't vitrify at 1450 which is problematic as if attmpting to vitrify loaded Clinoptilolite which has Cs in it this could have a detrimental effect on the wasteform. As a result, a scoping test was done for time effectiveness.

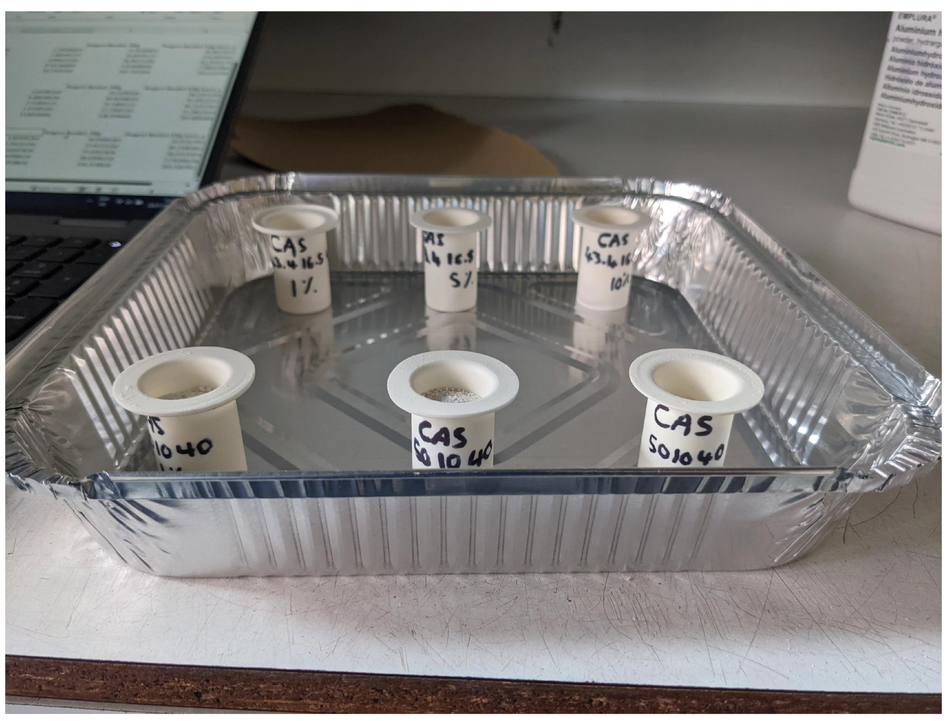

• This gave an insight into what the system required to form a melt with all 5 glasses being attempted at 1, 5 and 10 Mol% Cs loading with mixed results.

• Melts were seen to go at low Cs loading but higher loadings inhibited melting.

• As can be seen above lighter group 1 elements go into the system well and the Rb melts, although, 10% failed the 5% one didn't indicating element size/ mass could play a role in inhibiting melt.

• Once these melts were conducted (also with a 1600 Rb and Cs loaded second attempt to get 6 glasses (only 10% Cs didn't go)) XRD and Raman analysis was conducted on all the samples.

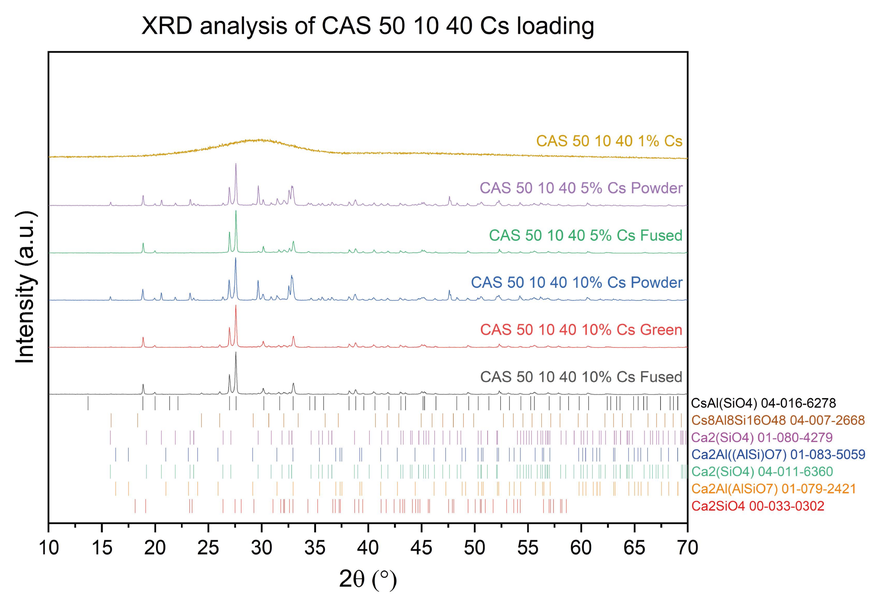

• XRD analysis indicated the formation of Pollucite and like minerals which are the Cs ore mineral and have some quoted melt T of 1900°C

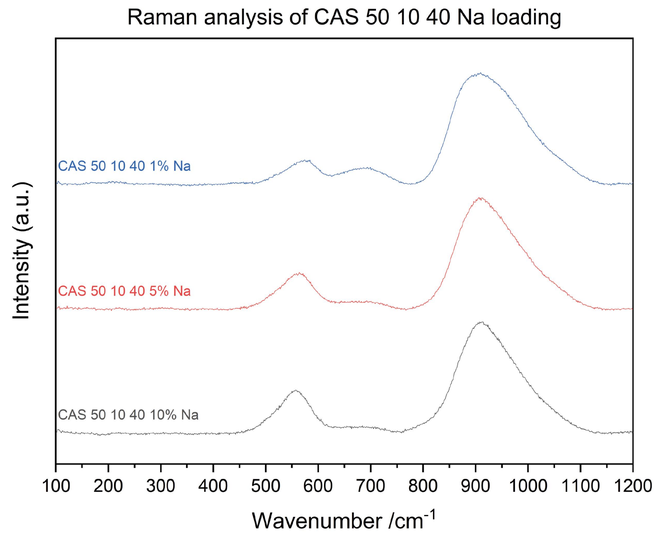

• When the alkalis went into the glass the Raman displayed a sharpening of the peak towards lower wavenumber around 925, a loss of the diffuse area around 700 and an increase in the signal seen at 550.